Energy-Banded Ions in Saturn's Magnetosphere

M. F. Thomsen[(1)], S. V. Badman[(2)], C. M. Jackman[(3)], X. Jia[(4)], M. G. Kivelson[(4,5)], and W. S. Kurth[(6)]

[(1)] Planetary Science Institute, 1700 East Fort Lowell, Suite 106, Tucson, AZ, 85719, USA

[(2)] Department of Physics, University of Lancaster, Lancaster, LA1 4YW, UK

[(3)] Department of Physics and Astronomy, University of Southampton, Southampton, SO17 1BJ, UK

[(4)] Climate and Space Sciences and Engineering, University of Michigan, Ann Arbor, MI, 48109, USA

[(5)] Earth Planetary and Space Sciences, University of California, Los Angeles, CA, 90095, USA

[(6)] Department of Physics and Astronomy, University of Iowa, Iowa City, IA, 52242, USA

Key Points

- First observation of energy-banded ions at Saturn
- Banded ions are H^+ but can not tell if other species are similarly banded
- Band energies are consistent with a bounce-resonant interaction with the standing wave of a field-line resonance

Abstract

Using data from the Cassini/CAPS ion mass spectrometer, we report the first observation of energy-banded ions at Saturn. Observed near midnight at relatively high magnetic latitudes, the banded ions are dominantly H+, and they occupy the range of energies typically associated with the thermal pick-up distribution in the inner magnetosphere (L<10), but their energies decline monotonically with increasing radial distance (or time or decreasing latitude). Their pitch angle distribution suggests a source at low (or slightly southern) latitudes. The band energies, including their pitch-angle dependence, are consistent with a bounce-resonant interaction between thermal H^+ ions and the standing wave structure of a field line resonance. There is additional evidence in the pitch-angle dependence of the band energies that the particles in each band may have a common time of flight from their most recent interaction with the wave, which may have been at slightly southern latitudes. Thus, while the particles are basically bounce-resonant, their energization may be dominated by their most recent encounter with the standing wave.

Introduction

The inner magnetosphere of Saturn is characterized by several different plasma populations [e.g., Young et al., 2005], including a dense, cool component that is locally produced by ionization of neutral water vapor vented by Saturn's moon Enceladus [e.g., Porco et al., 2006; Waite et al., 2006; Sittler et al., 2008], and a suprathermal, more-tenuous component that is primarily injected from the outer magnetosphere in discrete, centrifugally-driven interchange events [e.g., Burch et al., 2005; Hill et al., 2005]. The

47 cool ion population is dominantly composed of water-group ions (O^+, OH^+, H_2O^+, and
48 H_3O^+, commonly denoted "W^+") and H^+, with a lesser contribution of H_2^+ [e.g., Sittler et
49 al., 2005; Thomsen et al., 2010], plus other minor ions such as N^+ and O_2^+.
50 Saturn's strong magnetic field, combined with good ionospheric conductivity,
51 couples the rapid planetary rotation to the magnetospheric plasma, which is observed to
52 flow with nearly the rigid corotational azimuthal velocity in the inner magnetosphere
53 (L<~10) [e.g., Sittler et al., 2005; Wilson et al., 2008, 2009; Thomsen et al., 2010; Livi et
54 al., 2014]. Ionization of neutrals in this environment results in new "pick-up" ions, which
55 occupy a ring in velocity space that convects with the near-corotational bulk flow speed
56 and has a ring speed equal to that bulk flow speed [e.g., Tokar et al., 2008]. Such
57 distributions thermalize rather quickly, resulting in a population with a thermal speed
58 comparable to the bulk flow speed, still convecting with the flow. The average energy-
59 per-particle of a pick-up ion population should thus be approximately twice $0.5m_iV_c^2$,
60 where m_i is the mass of the ion, and V_c is the bulk flow speed of the plasma. Voyager
61 and typical Cassini observations [e.g., Bridge et al., 1981; Young et al., 2005] do indeed
62 show two peaks in energy-per-charge space, located just above the corotational energy
63 for H^+ and W^+, and rising with increasing radial distance as V_c itself rises (since $V_c \sim r\Omega_S$,
64 where Ω_S is Saturn's angular velocity).
65 While the relative fractions of thermal W^+ and H^+ vary with latitude because the
66 heavy ions tend to be centrifugally confined more closely toward the equatorial plane
67 than are the light ions [e.g., Thomsen et al., 2010], the two-peaked structure of the ion
68 E/q spectrum (with the energy of the peaks increasing with radial distance) is seen during
69 almost every Cassini pass through the inner magnetosphere. In this paper we report

70 observations from one of the rare exceptions to this rule: On 3 May 2005, as Cassini was
71 outbound through the near-midnight sector at a magnetic latitude ~20˚, the cool ion
72 distribution was observed to consist of ~3-4 discrete bands in E/q. The band energies
73 uniformly decreased with increasing radial distance, but they appeared superimposed on a
74 background thermal population that followed the expected general increase with r. The
75 bands persisted over at least 4 hours, as Cassini covered the radial range from L~5.6 to
76 7.5 (where L is the equatorial crossing point in Saturn radii, R_S, of a dipole field line
77 through Cassini's position) and the latitude range from ~21.8˚ to 18.1˚.
78 Energy-banded ions have been seen under a number of different circumstances in
79 the Earth's magnetosphere [see Colpitts et al., 2016, for a review]. They have been
80 reported during both quiet and geomagnetically active intervals; in the auroral zone, at
81 subauroral latitudes, and near the dayside magnetopause; and at ion energies of 10's of
82 eV to 10's of keV. In some cases composition measurements show that O^+ and H^+ bands
83 have the same energy, while other occurrences show O^+ and H^+ having the same
84 velocities. Still other studies show that O^+ and H^+ have different occurrence probabilities
85 and locations. In some observations the ions are peaked at 90˚ pitch angles, whereas in
86 others they appear dominantly field-aligned. Events can be very long-lasting, up to 12
87 hours, and often are extensive in both latitude and magnetic local time.
88 A number of possible generation mechanisms for energy-banded ions at Earth
89 have been proposed [also reviewed by Colpitts et al., 2016], including convective drift
90 dispersion or time-of-flight dispersion from either an ionospheric or an equatorial heating
91 event. The different generation scenarios have different implications for the properties of

92 the banded ions, and some observational support seems to exist for essentially all of the
93 mechanisms.
94 While energy-banded ions of various properties are well-documented in the
95 Earth's magnetosphere, no such phenomena have yet been reported in the giant
96 magnetospheres of Jupiter and Saturn. The purpose of the present paper is to report the
97 observation by Cassini of such an event in Saturn's inner magnetosphere and to examine
98 the properties of the banded ions.
99
100 Observations
101 The observations presented in this study come primarily from the Cassini Plasma
102 Spectrometer (CAPS) instrument on the Cassini spacecraft, which has been in orbit
103 around Saturn since mid-2004. CAPS consists of three separate sensors: the ion beam
104 spectrometer (IBS), the electron spectrometer (ELS), and the ion mass spectrometer
105 (IMS) [see Young et al., 2004, for details on the instrumentation]. In this report we focus
106 on data from the IMS, which is a top-hat electrostatic analyzer to measure the energy per
107 charge of incident ions, followed by a time-of-flight (TOF) section to determine their
108 speed and hence their mass per charge. The instantaneous field of view (FOV) of the
109 IMS is segmented into 8 separate angular channels viewing different directions in
110 velocity space. Under normal operating conditions, a physical actuator on CAPS sweeps
111 the FOV across the sky, resulting in solid-angle coverage of ~2π sr for the full actuation
112 cycle.
113 The IMS produces several different data products with different cadences that are
114 determined by the telemetry rate. "Singles" data (SNG) are obtained from the start

115 signals in the TOF section, so they yield only the energy per charge of the ions and not
116 their mass. They do, however, provide information about the angular distribution of the
117 particles. SNG data cover 64 contiguous, logarithmically spaced energy channels
118 between ~1 eV and ~50 keV for each of the 8 IMS anodes, summed over an actuation-
119 angle range that depends on the telemetry.

120 The TOF data provide mass determination, but because of the lower efficiency for
121 this measurement, the TOF data product is summed onboard over all look directions (all
122 8 detectors and all actuation angles) for either 512 s or 256 s, depending on the telemetry.
123 The ion distribution is further summed in energy, reducing the native 64 channels to 32.
124 A TOF data product therefore consists of counts in a matrix of 32 E/q levels by 256 time-
125 of-flight channels, enabling identification of the m/q of the various particles but no
126 information about their angular distribution.

127 Whenever a TOF data product is reported, CAPS also reports an ION data
128 product, which involves an onboard sorting of the counts into m/q bins based on the
129 measured E/q and TOF, much as is done on the ground with the TOF data product [e.g.,
130 Thomsen et al., 2014]. The ION data product is similar to the SNG product in that the
131 energy spectrum is reported for each of the 8 anodes, providing information on the
132 angular distribution of each species, but the count rates are typically quite low unless the
133 fluxes are very high. We are able to make only limited use of this capability in the
134 present study.

135 In addition to the CAPS data, we will present corresponding observations from
136 the Cassini magnetometer (MAG) [Dougherty et al., 2004] and the Radio and Plasma
137 Wave Investigation (RPWS) [Gurnett et al., 2004].

138 Figure 1a shows IMS observations for a typical low-latitude, nightside pass
139 through Saturn's inner magnetosphere. The panel shows the color-coded SNG count rate
140 from IMS anode 1 for 3.5 hours during an inbound pass on 16 Oct 2010. Between 0900
141 and 1300 UT, Cassini moved from L~7.00 to L~5.25, at a magnetic latitude ~-1° to -2°
142 and a local time of ~01-03 LT (c.f., Figure 2, black curve). The count rate is shown as a
143 function of the ion E/q on the vertical axis and time on the horizontal axis. The solid
144 black line superimposed on the spectrogram shows the local corotational energy of a
145 proton ($0.5 m_p \rho^2 \Omega_S^2$), where $\rho = r \cdot \cos\lambda$, with λ the latitude of the spacecraft and r its radial
146 distance from Saturn. The W^+ corotational energy would be a factor of ~16 above the H^+
147 value shown in the figure. The ion spectra in Figure 1a exhibit a double-peaked character
148 in E/q. As described above, the two peaks correspond to H^+ (below ~100 eV/e) and W^+
149 (above ~100 eV/e). As expected for thermalized pick-up ion distributions observed with
150 an electrostatic analyzer, the peak count rates (proportional to the energy flux) are found
151 near 4 times the corotational energy of each species, decreasing as the spacecraft
152 approaches Saturn. The periodic variations in the count rate are produced as the actuator
153 scans the FOV of the instrument through different look directions.
154 During the interval in Figure 1a, CAPS was able to view the corotational direction
155 of motion, so the bulk of the trans-sonic distribution lies within the FOV, accounting for
156 the high count rates. At these low latitudes, W^+ dominates the E/q spectra because it is
157 more confined to the magnetic equator by centrifugal force than is the H^+ [e.g., see the
158 species-dependent scale heights derived by Thomsen et al., 2010]. But the two-peak
159 character of the E/q distribution is quite clear.

Figure 1b shows a similar spectrogram for a typical higher-latitude inbound pass near dawn on 9 Sep 2006, in this case from anode 7. During the interval shown, the spacecraft moved from (L,λ,LT) of (7.0, -18.9˚,5.5) to (5.5,-23.4˚,7.0) (see Figure 2, blue curve). Again the viewing was favorable for seeing the corotating trans-sonic distribution, with periodic variations due to the actuation of the instrument. Due to the higher latitude, W^+ is no longer the dominant ion in the spectrogram, with the H^+ peak (lower energies) as intense or even more intense than the W^+ (upper energies). As in Figure 1a, it is clear that the ion populations peak at E/q near and above their corresponding corotational energies, decreasing with declining distance from the planet. (The spectral event near 1020 UT is an example of the centrifugally-driven interchange injection events mentioned in the introduction and is not relevant to the present discussion.)

Figure 1c shows a third spectrogram, from anode 1 for an outbound pass on 21 May 2005, during which Cassini moved from (L,λ,LT) of (5.5, 22˚,23.8) to (6.9,19˚,1.3) (see Figure 2, green curve). For this interval, CAPS was not actuating and did not view directly into the corotational direction. There are numerous interchange injections, but the cool plasma is still visible between events. There is little cool W^+ observed due to the high latitude and poor viewing, but the energy of the cool H^+ tracks the corotational energy quite well, increasing with increasing radial distance, as was the case for the other intervals shown in Figures 1a and 1b (in this case, since the instrument was looking essentially perpendicular to the flow, the peak count rate is seen at less than four times the corotational energy, as one would expect).

182 Finally, Figure 1d shows a spectrogram from anode 1 obtained on 3 May 2005,
183 during which Cassini was outbound through the same general L range as the other panels
184 in Figure 1, moving from (L,λ,LT) of (5.4, 22˚,23.7) to (7.7,17˚,2.0) (see Figure 2, red
185 curve). On this pass, which immediately preceded the pass shown in Figure 1c and had
186 very similar orbital parameters, the ion E/q distribution looks quite different from that
187 seen on the previous orbit. CAPS was again not actuating, but prior to 0630 UT, anode 1
188 was looking only slightly off the corotation direction, and strong fluxes were seen in both
189 the H^+ and W^+ populations, with H^+ dominating at this high latitude. During this interval,
190 the E/q distribution showed two peaks, corresponding to corotating pick-up H^+ and W^+,
191 as in the other panels. After 0630 UT, the spacecraft executed a roll such that neither
192 anode 1 nor any of the other anodes was viewing near the corotation direction, and the
193 fluxes dropped accordingly. Further, with the anodes now looking well away from
194 corotation, a different energy structure appears in the distribution: There are now 3
195 distinct bands of ions, with energies that decrease with increasing radial distance instead
196 of increasing in correspondence with the corotational energy. Moreover, at ~0800 UT
197 the bottom energy band disappears and is replaced by an additional band above 100 eV.
198 This disappearance of the lowest-energy band and replacement with a new highest-
199 energy band was repeated at least once more before ~1040 UT, when another spacecraft
200 roll moved the IMS FOV into the direction opposite corotation, and the fluxes became
201 quite low. All of these bands occupy the same general range of energies occupied by the
202 thermal plasma at lower latitudes (c.f., Figures 1a and 1b), but the band energies clearly
203 decrease with time and increasing radial distance. The bands seem to disappear when the

204 band energy falls below the local corotational energy (black line). The peak-to-trough
205 flux amplitudes of the bands are ~few-20%.
206 Figure 3 focuses on this interval from 3 May 2005 in more detail, with views from
207 4 anodes presented in 4 separate panels. As shown there, the level of the fluxes
208 decreased for progressively higher anode numbers, which correspond to view directions
209 closer to the magnetic field. Anodes 5-8 likewise saw the bands, but at even lower
210 fluxes. A detailed examination of the count-rate E/q spectra (not shown) reveals that the
211 peaks are not seen at exactly the same energy in the various anodes; rather, there is a
212 slight but systematic and progressive shift in energy from anode 1 to the other anodes.
213 We will return to this point below when we discuss the pitch-angle distribution of the
214 banded ions, but we bring it up here because it has implications for analysis of the
215 composition of the bands, to which we turn next.
216 As described above and in greater detail by Thomsen et al. [2014], the TOF data
217 product enables determination of the composition of the ions measured by CAPS, albeit
218 with no angular information and with reduced energy resolution. Figure 4 shows the
219 energy distribution of the counts in the three main ion species (H^+, H_2^+, W^+) for a
220 representative interval during the banded ion event, computed following the procedure
221 described in Thomsen et al. [2014]. The two vertical bars span the range of energies of
222 the highest-energy clear peak in the SNG spectrum for all the anodes over this time
223 range. The other clear peaks were all at lower energies than these bars, and it is clear
224 from the figure that in the range of energies where the bands are observed H^+ is by far the
225 dominant contributor to the counts. There is a small peak between the vertical bars in
226 Figure 4, but the band structure is far from obvious, first because the TOF product sums

227 over two adjacent energy channels, so the energy resolution is intrinsically lower than for
228 SNG data, and second because the TOF product sums over all the anodes, which as noted
229 above see the band peaks at slightly different energies, further smearing the structure in
230 energy. Nonetheless, from Figure 4 it is clear that the bands that are seen in SNG are
231 primarily in the H^+ population. There may also be bands in the other species, but the
232 energy resolution of the TOF data product is not adequate to say definitively whether or
233 not this is the case. Examination of the ION data product mentioned above (not shown)
234 confirms that the onboard-sorted H^+ does in fact display the same peaks as the SNG
235 spectra, but with much lower count rates. The count rates in the ION W^+ and H_2^+ spectra
236 are too low to draw meaningful conclusions about whether or not bands exist in those
237 species.
238 Returning to the energies of the bands, it is important to realize that these are the
239 particle energies as seen in the frame of the spacecraft. Since the plasma is
240 approximately corotating with Saturn, it is necessary to transform into the corotating
241 frame to examine the true band energies and pitch angles. Ideally, one would transform
242 into the plasma rest frame, but because the actuator was not operating during this interval,
243 we are unable to obtain bulk flow moments of the distribution [e.g., Thomsen et al.,
244 2010] and have simply assumed full corotation to do the transformation. While several
245 studies have shown that the flow speed in this region of the magnetosphere is actually
246 more typically ~60-90% of full corotation [e.g., Wilson et al., 2008, 2009; Thomsen et
247 al., 2010; Holmberg et al., 2012], the assumption of full corotation as opposed to 60%
248 makes only a small quantitative difference (few degrees in pitch angle, few percent in
249 energy). The SNG measurements have accordingly been transformed to the corotating

250 frame, and the energies of the peaks in that frame have been tabulated at 15-minute
251 intervals during the 3-h period from 0630 to 0930 UT.

252 Figure 5 summarizes the resulting band energies in the corotating frame. Panel a
253 shows the band energies for the four anodes with the highest counting rates, plotted as a
254 function of time during the 3-h interval. Even in the corotating frame, it is clear that the
255 band energies vary with look direction. The solid line in Figure 5a is the H+ corotation
256 energy over the same time range, showing the increase with time that contrasts clearly
257 with the decrease seen in the band energies. Figure 5b shows the band energies as a
258 function of time for just anode 1, which has the highest count rates. The bands show a
259 very clear and near-exponential decrease with time during the interval. Because of the
260 nature of Cassini's orbit at this time, both the L value and the latitude of the spacecraft
261 varied monotonically with time, and Figures 5c and 5d show the anode 1 band energies
262 plotted as a function of L and latitude, respectively. These also yield nearly exponential
263 dependences of the band energies, decreasing with L and increasing with latitude. The
264 coupling of these parameters makes it impossible to determine which dependence is
265 primary (t, L, or λ). Table 1 provides the coefficients of exponential fits to the three
266 parameters for the three anode-1 bands highlighted in Figures 5b-5d. Based on these fits
267 for anode 1, the average ratio of the band 2 (middle) energy to the band 1 (lowest) energy
268 is ~2.0, and the average band 3 (highest) to band 2 ratio is ~2.5.

269 In addition to calculating the band energies in the corotating frame, we have also
270 calculated the pitch angles seen by each of the anodes in this frame. We have then
271 binned the observed counts into energy and pitch angle bins for 5-min intervals during
272 the pass. Panels a, b, and c of Figure 6 show the count rate as a function of energy and

pitch angle bin for three different 5-min intervals during the time when the ion bands were seen. The bands can be seen in each panel; moreover, all three panels show that the energy of the bands appears to decrease with increasing pitch angle, even across 90˚. This is confirmed by Figures 6d, 6e, and 6f, which show the band energies vs pitch angle for three of the individual spectra summarized in Figure 5a. In Figures 6d, 6e, and 6f, we have connected points corresponding to the same apparent band in order to guide the eye, but the bands clearly follow the same behavior seen in the 5-minute summed pitch-angle plots in Figures 6a, 6b, and 6c. Note that for Cassini's location at northern latitudes at this time, particles with pitch angles less than 90˚ are moving toward the equator, whereas those with pitch angles greater than 90˚ are moving away from the equator.

Further, Figures 6a, 6b, and 6c show that the energy flux (proportional to the color-coded counts) is greater for particles coming from the equator (p.a.>90˚) than for those coming from high latitudes (p.a.<90˚) at the same |p.a.-90˚|.

Discussion

Other events

We have not conducted a comprehensive survey for additional such banded-ion events, but Table 2 lists the few intervals where we have seen banding while surveying the data for other purposes. None of these additional intervals shows the bands quite as clearly as the 3 May 2005 event described above, nor have we done such a complete analysis of the band properties in those events. For the remainder of this paper, we focus on the 3 May 2005 event, but the other events may yield additional relevant information in the future.

296

297 *Transport of banded ions*

298 In addition to the observational features described above regarding the banded
299 ions, consideration of the band energies (in the corotating frame) provides additional
300 insight. We focus first on locally mirroring particles (i.e., with pitch angles of 90˚). We
301 obtain the band energies for those particles by interpolating along energy-vs-pitch-angle
302 curves such as those shown in Figure 6d, 6e, and 6f. Using a dipole approximation for
303 the magnetic field, which is valid within the radial range of interest [Burton et al., 2010],
304 we estimate the equatorial pitch angle corresponding to locally mirroring particles.
305 Combining the equatorial pitch angle and the inferred band energy for locally mirroring
306 particles, we estimate the travel time from the equator to the observation point for H^+ ions
307 at each of the 15-minute intervals shown in Figure 5. For locally mirroring particles this
308 is just ¼ bounce period, where the latter is calculated according to Thomsen and Van
309 Allen [1980]. The results are shown in Figure 7a for four identifiable bands, with Band 1
310 being the lowest-energy one.

311 Subtracting this direct travel time from the time of observation, we find the most
312 recent time at which particles in each band would have left the equator on their way to
313 the spacecraft. These equatorial departure times (in sec of the day) are shown in Figure
314 7b. This calculation reveals that the slowest particles seen by Cassini at 0645 UT (band
315 1) left the equator at ~0530 UT, while particles in the most energetic band seen at 0645
316 (band 3) left the equator at ~0608 UT. Assuming full corotation (and ignoring gradient
317 and curvature drifts, which are negligible in this energy range), the direct travel times
318 combined with the local time of observation also determine the local time at which the

319 banded ions left the equatorial plane. These are shown in Figure 7c. Note that although
320 the energy-banded ions were observed by Cassini near local midnight, the travel time
321 from the equator is so long for these energies that the original departure from the equator
322 actually occurred near LT~21 for the lowest-energy band.

323 Finally, Figure 7d shows the difference in the equatorial departure time between
324 pairs of adjacent bands. At least for the lowest 3 bands (1-3), the inferred departure times
325 are separated by ~1200-1700 s, apparently increasing with time or radial distance.

326 The solid line shown in Figure 7d is the travel time for an Alfvén wave to
327 propagate along the field line from the equator to a high-latitude mirror point and back to
328 the equator. To find this time, we combined the radial dependence of the equatorial
329 densities of the three main ion species determined by Thomsen et al. [2010] and shown in
330 their Figure 7c with the scale heights also given in that figure to calculate the plasma
331 mass density as a function of latitude along a given dipole magnetic field line in the inner
332 magnetosphere. The corresponding Alfvén speed as a function of L and λ was then
333 calculated, and the travel time was integrated over one half the bounce period, yielding
334 the curve shown in Figure 7d.

335

336 *Possible scenario: Field Line Resonance*

337 The half-bounce Alfvén time in Figure 7d is of the same order as the time
338 difference between successive equatorial departure times for the banded ions, and it has
339 the same radial dependence. This suggests that the bands may be produced by
340 acceleration/deceleration within a large-scale field line resonance (FLR). FLRs are
341 standing shear Alfvén waves with parallel wave numbers that are quantized by the

342 ionospheric boundary conditions [e.g., Chen and Hasegawa, 1974; Southwood, 1974;
343 Kivelson and Southwood, 1985; Hughes, 1994]. The fundamental mode (n=1) has one
344 half wavelength between ionospheric boundaries, and the second harmonic (n=2) has a
345 full wavelength between ionospheric boundaries. The corresponding eigenfrequencies
346 are therefore approximately $f=nV_A/2S$, where V_A is the Alfvén speed near the equator and
347 S is the length of the field line. Thus, the period of the fundamental mode is the Alfvén
348 bounce period on the field line, while the second harmonic period is half that bounce
349 period. FLRs are commonly observed at Earth, and a large literature exists in which their
350 properties, causes, and consequences have been explored. Recently, Yates et al. [2016]
351 showed Cassini magnetic field observations that provide persuasive evidence that field
352 line resonances occur in Saturn's outer magnetosphere and may be responsible for the
353 ~1-hour periodicities that have been reported in a number of magnetospheric properties at
354 Saturn, including energetic particle fluxes, magnetic field, plasma wave emissions, and
355 the aurora [see Palmaerts et al., 2016, and references therein]. Yates et al. [2016]
356 concluded that their high-latitude magnetic field observations were most consistent with
357 second harmonic Alfvén waves on closed outer magnetospheric field lines with plasma
358 density concentrated near the equator.

359 Charged particles interacting with the wave fields of FLRs can gain or lose energy
360 depending on the wave phase, the energy distribution of the particles, and spatial
361 gradients in the phase space density. The theoretical basis for such particle energization
362 was explored by Southwood and Kivelson [1981, 1982], and recent test-particle
363 simulations for conditions at Earth confirm the expected energization [Rankin et al.,

2016]. The concept has also been successfully applied to particle observations at Earth [e.g., Yang et al., 2011a,b; Zong et al., 2012; Ren et al., 2016].

In the Southwood and Kivelson analysis, there are two modes of energization: 1) a resonant or near-resonant acceleration/deceleration of particles gradient/curvature drifting parallel to the wave electric field, and 2) an adiabatic acceleration/deceleration of particles displaced in L by ExB drifts in the wave electric field. The effect on the flux of particles of a given energy of these two processes can be expressed as

$$\frac{\delta f}{f} = \frac{1}{f}\frac{\partial f}{\partial E}\bigg|_L \Delta E + \frac{1}{f}\frac{\partial f}{\partial L}\bigg|_\mu \Delta L \qquad 1)$$

where

$$\Delta E = q v_D \mathcal{E}_\varphi \Delta t \qquad 2)$$

$$\Delta L = c\frac{\mathcal{E}_\varphi}{BR_s}\Delta t \qquad 3)$$

Here f is the phase space density of the particle distribution (proportional to flux/energy), $\mathcal{E}$ is the wave electric field, v_D is the gradient/curvature drift speed of a particle, B is the ambient (presumed dipole) magnetic field strength, R_s is the radius of Saturn, and Δt is the time the particle is exposed to the wave.

The energization and radial transport indicated by Equations 2 and 3 depend on the sign of the azimuthal component of the electric field [e.g., Southwood and Kivelson, 1981] and in general tend to average to zero as particles bounce in a time-varying field. However, for certain resonant bounce frequencies, the particles repeatedly encounter the wave field in the same orientation, leading to accumulated acceleration (or deceleration). Since the phase space density of the particles decreases with energy, there are more particles available to gain energy than to lose energy, so particles with a resonant bounce

386 frequency will exhibit a flux enhancement over multiple bounces. The resonant bounce
387 periods are integer multiples of the wave period. Hence, for particles interacting with
388 field line resonances, we would expect flux enhancements at energies corresponding to
389 bounce periods of

390 $$T_b = mT_w = mT_{Ab}/n \quad (4)$$

391 where m is the order of the particle resonance, n is the field-line resonant mode number,
392 and T_{Ab} is the Alfven wave bounce period.

393 Figure 8 shows a comparison of the bounce periods computed for locally
394 mirroring protons at the observed band energies and various harmonics of the Alfvén
395 bounce period as given by Equation 4 for n=1 and n=2. The Alfvén bounce times were
396 computed as described above. Allowing for uncertainties in the equatorial density
397 distribution and the plasma scale heights, the left-hand side of Figure 8 (n=1) shows
398 fairly good agreement between the band-ion bounce periods and low orders of the Alfvén
399 bounce period. The right-hand side of Figure 8 shows that it would require rather high
400 orders (m) to match the observed particle bounce periods in n=2 and that a number of
401 orders would be missing. However, there are uncertainties in both the equatorial
402 densities and scale heights used above that would probably allow a longer Alfvén bounce
403 period, so we can not rule out a match for n=2. Similarly, even at these relatively low L
404 values there is significant field-line stretching due to Saturn's ring current, which also
405 tends to increase T_{Ab}. Thus, we conclude that the band-ion bounce periods are consistent
406 with the fundamental or second harmonic FLR.

407 Assuming a Maxwellian hydrogen distribution with density and temperature as
408 determined by Wilson et al. [2008], we can estimate the magnitude of the terms in
409 Equation 1. For an Alfvén wave,

410 $$\mathcal{E}_{\varphi} = (v_A / c) \cdot \delta B \qquad 5)$$

411 where δB is the magnetic perturbation of the wave, and the equation relates only the
412 amplitudes of the electric and magnetic field perturbations, which are actually
413 orthogonal. Guided by the measurements of Yates et al. [2016], we adopt δB=0.3 nT and
414 Δt=1800 s and find that for an H+ energy of 30 eV at L=6, Equation 1 gives

415 $$\frac{\delta f}{f} = 0.009 + 0.018 = 0.027 \qquad 6)$$

416 Thus, a very crude estimate of the effect a field line resonance might have on the
417 hydrogen flux is ±3% for a single encounter with the wave. Multiple encounters by
418 resonant particles would increase this energization. Given that we don't actually know
419 the wave amplitude encountered by the particles, nor its latitude dependence, this is
420 plausibly close to the value of ±few-20% observed between the band peaks and the
421 troughs between them.
422
423 *Pitch Angle Dependence*
424 One prediction of such a scenario is that the band energies seen at Cassini should
425 vary with pitch angle since it is the parallel component of the particle velocity that
426 determines the bounce frequency. Assuming conservation of particle energy and
427 magnetic moment as ions travel along the magnetic field from the equator to the
428 observation point, one can calculate the energy as a function of local pitch angle for

429 which the bounce periods are equal to those shown for locally mirroring particles in
430 Figure 5a. The result is given in Figure 9a for the CAPS observation at ~0700 UT
431 (L~5.9, λ~21˚), overlaid on the observed pitch angle dependence of the band energies
432 shown in Figure 6d. While there are clear quantitative discrepancies between the model
433 pitch angle dependence and the observed variation, the qualitative tendency for the band
434 energy to decrease with increasing pitch angle is reproduced.
435 The one qualitative discrepancy in Figure 9a is that above 90˚, the observed band
436 energies continue to decrease, whereas the energies for constant bounce period begin to
437 increase again. This decrease in the band energies across 90˚ pitch angle is a persistent
438 feature of the banded ions, as shown in Figure 6. As noted above, particles with pitch
439 angles greater than 90˚ are those that are moving away from the equator, whereas those at
440 pitch angles less than 90˚ have mirrored at latitudes above the spacecraft and are
441 returning toward the equator. Thus, the particles with pitch angles greater than 90˚ have
442 travelled a shorter distance since their last equatorial encounter than have particles on the
443 descending part of their bounce (pitch angles less than 90˚). They have also more
444 recently passed through the latitude range below the spacecraft, and it is possible that
445 they have encountered the wave there in a different phase, leading to deceleration rather
446 than acceleration.
447 On the other hand, the discrepancy in the behavior of the band energy across 90˚
448 shown in Figure 9a might be an indication that, while the particles are resonant with the
449 wave, what counts most in determining their current state of acceleration/deceleration is
450 the phase of the wave when the particles most recently encountered it. Thus, at any given
451 time the spacecraft will see enhanced fluxes only for particles whose time of flight was

452 such that they encountered the wave region at the right phase, i.e., there will be a discrete
453 energy band corresponding to particles with the right time of flight. This possibility
454 suggests that the bands may correspond to constant times of flight, rather than just
455 constant bounce period. Figure 9b shows the pitch-angle dependence of the observed
456 band energies for the same interval as Figure 9a, overlaid on the energy as a function of
457 local pitch angle for which the times of flight from the equator to the spacecraft are equal
458 to those for locally-mirroring band particles. Again there are clear quantitative
459 discrepancies between the model pitch angle dependence and the observed variation, but
460 the qualitative tendency for the band energy to decrease with increasing pitch angle is
461 reproduced, including across 90˚.
462 The agreement between the observed pitch angle dependence of the band energies
463 and the modeled dependence can be improved by changing the presumed origin of the
464 accelerated particles (i.e., the region along the field where the particles encountered large
465 wave amplitudes in the correct direction). Figure 9c shows the same calculation as
466 Figure 9b, except that the ions are assumed to be traveling from a magnetic latitude of
467 -20˚. (Note that in order to yield particles that mirror locally at Cassini, the launch
468 latitude must be less than or equal to the spacecraft latitude.) The energy/pitch angle
469 dispersion in the modeled bands now matches the observations much better than for an
470 equatorial origin.
471 The possibility that the energization of the resonant or near-resonant particles
472 might be dominated by their most recent encounter with the wave is not unreasonable in
473 light of the very long bounce periods of the resonant particles (>2 h, see Figure 7d). To
474 be truly “bounce resonant”, particles would need to encounter the wave on multiple

475 bounces, always in the right wave phase. For such long bounce periods, this would
476 require that the wave properties stay stable over close to a planetary rotation. Thus, any
477 local time dependence to the plasma or field properties would tend to wash out some of
478 the earlier resonant behavior, but would leave the most recent wave encounter intact.
479 Figure 10 is similar to Figure 7 but is constructed under the assumption that the
480 prime acceleration point for the particles was at a latitude of -20˚. From this location, the
481 travel times would be considerably longer, the prime acceleration times considerably
482 earlier (~4.6 UT vs ~5.7 UT for an equatorial source), and the local time of origin
483 considerably earlier (near dusk vs ~21 LT for an equatorial source). The difference in
484 departure times for the subsequent energy bands is also longer, now somewhat greater
485 than half the Alfven wave bounce time. We have not attempted to optimize the match to
486 the wave bounce time, but it is clear from Figures 7d and 9d that a source location
487 between the equator and λ~-20˚ would probably bring them fairly close together.
488 The problem with attributing the bulk of the particle energization to the most
489 recent wave encounter is that the few percent increase in flux estimated above in
490 Equation 6 would not be adequate to give the observed flux modulation based on a single
491 wave encounter. To get enough energization in a single encounter, the wave amplitude
492 would have to be much larger than assumed above. Since we don't actually know what
493 the wave amplitude is in the prime acceleration region, we simply leave this as a puzzle
494 for future consideration.
495
496 *Possible Sources of FLR: Dynamic Pressure Impulse*

497 In the terrestrial magnetosphere, field line resonances not uncommonly originate
498 from a dynamic pressure impulse imparted by the solar wind, such as an interplanetary
499 shock [e.g., Southwood and Kivelson, 1990]. The initial impulse propagates through the
500 magnetosphere as a fast-mode compressional wave, which couples to shear mode Alfvén
501 waves that form the field line resonances [e.g., Tamao, 1964; Chen and Hasegawa, 1974;
502 Southwood, 1974; Lysak and Lee, 1992; Chi et al., 2006]. Such conversion occurs
503 primarily in regions of strong gradients of the Alfven velocity (such as the Earth's
504 plasmapause).
505 If the banded ions seen by Cassini on 3 May 2005 are due to the passage of a
506 compressional wave front and energization by the standing waves it produces by coupling
507 to a field-aligned wave mode, then we need to ask if there is other observational evidence
508 for the passage of such a compressional wave or the existence of the field-line resonance.
509 Figure 11 presents three types of data that are potentially useful for this question: a) the
510 magnetic field magnitude and azimuthal component measured by Cassini in the hours
511 before and during the banded ion observations [Dougherty et al., 2004]; b) the electric
512 wave spectra observed by the RPWS instrument during the 2-day interval encompassing
513 the banded ion event, plus 2-day intervals from the previous and subsequent periapsis
514 passes [Gurnett et al., 2004]; and c) a 50-day interval of solar wind properties projected
515 to Saturn's location via the mSWIM MHD model [Zieger and Hansen, 2008].
516 In Figure 11a, the interval corresponding to the backward projected departure
517 times of the lowest energy band of ions is shown as the solid black bar above the panel.
518 The range of this bar covers the range of ion departure times both for an assumed
519 equatorial encounter with the wave and one at -20˚ latitude, and any passing

520 compressional wave would presumably be found somewhere near this time. The dashed
521 bar just to the right of the solid bar indicates the range of times over which field line
522 resonances would be expected.
523 Examination of the upper panel of Figure 11a reveals no indication of a magnetic
524 field compression occurring near the solid bar or any other time during the 10-hour
525 interval displayed. Subtraction of a dipole model to examine residual field (not shown)
526 also does not show significant evidence of compression. Any variations in the field
527 strength are at less than the 1% level throughout. Magnetic compression signatures have
528 previously been reported in Saturn's lobes [e.g., Jackman et al., 2010; Thomsen et al.,
529 2015] but not within the inner magnetosphere (other than those associated with
530 interchange injection events). However, observations of compressional pulses launched
531 into Earth's magnetosphere suggest at least three possible considerations that might make
532 it difficult to detect compressions at Cassini's location at this time: The first is that
533 Cassini was located near midnight local time during the interval when a compressional
534 signal might have been propagating through the region (c.f., Figure 11a), and numerous
535 studies at the Earth (particularly at geosynchronous orbit, L=6.6) have shown that the
536 geomagnetic field response to sharp solar wind dynamic pressure variations is typically
537 very weak to nonexistent on the night side [e.g., Borodkova et al., 2005; Wang et al.,
538 2007; Villante and Piersanti, 2008; Jackel et al., 2012]. The second consideration is that
539 Cassini was at very low L values (~4) at the time a compression might have been
540 expected. Since the magnetic field there is quite large, one might not expect to observe a
541 significant compressional signature. Finally, the third consideration is that Cassini was
542 also at a relatively high latitude (~20˚); information about the latitude dependence of the

543 compressional signals at Earth doesn't seem to be available in the literature (except at
544 ionospheric altitudes), but it seems possible that the compressional signature may be
545 largely confined to the near-equatorial region. Moreover, measurements from a global
546 MHD simulation of Saturn's magnetospheric response to a solar wind dynamic pressure
547 enhancement [Jia et al., 2012] show a compressive signal less than 1% of the ambient
548 magnetospheric magnetic field at L=6, LT=23 and latitude =20˚ (X. Jia, unpublished
549 analysis). The small amplitude of the signature, combined with the decreasing relative
550 amplitude as the background field increases between L=6 and L=4, suggests that Cassini
551 may well not have been able to detect a tiny compression this deep in the magnetosphere
552 at a latitude of 20˚.

553 The lower panel in Figure 11a shows the azimuthal component of the magnetic
554 field observed at Cassini through this time period. High-frequency fluctuations visible in
555 the figure after ~05:30 UT may be electromagnetic ion cyclotron waves, which are
556 ubiquitous in the ion-pickup region of Saturn's inner magnetosphere [e.g., Leisner et al.,
557 2006; Russell et al., 2006]. Between about 00:30 and 05:30 UT the instrument was
558 operating in a higher dynamic range, and the interval of sharply higher fluctuation
559 amplitudes then is due to the digitization level in that range. In addition to these high-
560 frequency signals, there are 3-4 enhancements in B_ϕ separated by ~40 minutes, as
561 indicated by the vertical bars in the panel. It seems possible that these could be the
562 signature of the field line resonances left behind on these field lines by the passage of a
563 compressional signal at an earlier local time (closer to 18 LT, see Figure 9).

564 While the magnetic field data of Figure 11a do not show any direct evidence of
565 the occurrence of a sudden compression of the magnetosphere, we can also look for a

566 signature in the observations of the RPWS instrument. Previous work has shown that
567 solar wind dynamic pressure enhancements characteristically lead to sudden brightenings
568 of Saturn Kilometric Radiation (SKR) emissions and the extension of SKR to lower
569 frequencies than its normal range [e.g., Desch, 1982; Kurth et al., 2005; Bunce et al.,
570 2005; Mitchell et al., 2005; Jackman et al., 2009, 2010; Thomsen et al., 2015]. Figure
571 11b presents RPWS electric field spectra for the two days surrounding the periapsis pass
572 on which the banded ions were seen (marked by the solid bars above and below the
573 center panel), as well as the two-day intervals surrounding the two periapsis passes
574 immediately preceding and following the one of interest here (upper and lower panels).
575 In these spectrograms, SKR emissions are seen as wave power above a few tens of
576 kilohertz, except in a "shadow zone" near periapsis where such waves are excluded [e.g.,
577 Galopeau et al., 1989; Lamy et al., 2008]. In comparing the inbound versus outbound
578 RPWS observations surrounding periapsis on day 123 (center panel), we find no evidence
579 for an enhancement in SKR intensity, nor an extension to lower frequencies, during the
580 time when our analysis above would predict the passage of the compressional wave
581 (~few hours after midnight on day 123). Indeed, comparison of the center panel in
582 Figure 11b with the upper and lower panels does not reveal any distinctive plasma wave
583 signature that might be attributed to the passage of a solar wind dynamic pressure
584 enhancement on day 123. There exists a possibility that if the SKR during the interval of
585 interest was dominantly from the southern source, the so-called shadow zone [Lamy et
586 al., 2008] might have prevented Cassini at relatively high northern latitudes from seeing
587 the emissions, but this should not have affected SKR observations beyond L~7. Thus,

588 SKR data do not appear to support the occurrence of a global compression early on day
589 123.

590 Finally, Figure 11c explores the possibility of a solar wind dynamic pressure
591 increase by reference to the solar wind parameters predicted at Saturn's orbit by the
592 MHD model mSWIM, constrained by 1 AU observations [Zieger and Hansen, 2008].
593 Figure 11c presents the predicted density, speed, and dynamic pressure at Saturn's
594 location between days 100 and 150 of 2005. The three periapsis intervals shown in
595 Figure 11b are indicated by the vertical dashed lines. The model predicts that early on
596 day 123 Saturn would have been in the low-speed, low-density rarefaction region
597 preceding the arrival of a high-speed stream early on day 124. The year 2005 was a good
598 one for mSWIM predictions in that it featured a high recurrence index of solar wind
599 properties [Zieger and Hansen, 2008], but unfortunately the interval of interest around
600 day 123 was quite far removed from the optimum near-opposition of Earth and Saturn,
601 for which the model predictions are most accurate (days 13-41 in 2005 [mSWIM
602 webpage http://mswim.engin.umich.edu/validation.php]). In Zieger and Hansen's 2008
603 study, for intervals ~100 days after near-opposition, there is considerable uncertainty in
604 the modeled shock arrival time, with both positive and negative time lags (prediction
605 later/earlier than actual arrival, respectively) up to 40 hours or so. Thus, it is possible that
606 the shock predicted by mSWIM on day 124 could have arrived early on day 123 at the
607 time expected according to the hypothesis we have advanced. RPWS saw no strong
608 enhancement of SKR or any low-frequency extensions on day 124 (not shown),
609 suggesting that the predicted pressure enhancement did not arrive on that day.

In summary, we find possible evidence for a field line resonance in a few B_ϕ enhancements seen in the same time frame as the banded ions, with time separations ~40 min, comparable to ½-1 times the Alfvén bounce period (c.f., Figure 10d). However, while the mSWIM model predicts a solar wind dynamic pressure enhancement on the following day, which would be within the uncertainty of the modeling, the observations in Figure 11 provide no clear magnetospheric evidence supporting the passage of a global compressional event early on day 123. Nonetheless, because compressional waves propagate in all directions relative to B, compressional perturbations are so spatially dispersed that even a small amplitude compression can have a significant effect on a global scale. A resonant flux tube extracts energy all along its extent from ionosphere to ionosphere and the locally small compressional perturbations can thus be a significant energy source for the standing wave resonance. So we can not fully rule out the possibility of a solar wind impulse as the stimulus for the FLR.

Possible Sources of FLR: Magnetopause Fluctuations

Another possible source for the inferred field line resonances is ongoing Kelvin-Helmholtz (KH) activity at the magnetopause or pulsed magnetopause reconnection, as have been found at Earth [e.g., Singer et al., 1977; Anderson et al., 1991; Engebretson et al., 1998; Le et al., 2004]. Evidence for KH waves at Saturn's magnetopause has certainly been reported in Cassini in situ data [e.g., Masters et al., 2009, 2010, 2012; Cutler et al., 2011; Wilson et al., 2012] and in small-scale structure in auroral emissions [Grodent et al., 2011]. A survey of magnetic signatures of KH at Saturn found that the occurrence frequency is highest on the dusk flank, contrary to previous expectations

633 [Delamere et al., 2013], but subsequent theoretical exploration of the KH instability at
634 Saturn confirmed that the dusk magnetopause should often be KH-unstable and that KH
635 is inhibited on the dawn side [Desroche et al., 2013]. The banded-ion observations
636 presented here seem to imply field line resonances on the dusk side, consistent with this
637 dusk preference for KH.
638 A number of recent Cassini observations have reported quasi-periodic variations
639 with periods ~1 hour in magnetospheric properties, especially the fluxes of energetic
640 particles, auroral broadening, auroral hiss, and the magnetic field [Roussos et al., 2016;
641 Mitchell et al., 2016; Palmaerts et al., 2016; Yates et al., 2016]. The statistical
642 occurrence of the quasi-periodic phenomena suggests a high-latitude source [Palmaerts et
643 al., 2016], and several authors have suggested that they originate in KH instability of the
644 magnetopause [Roussos et al., 2016; Mitchell et al., 2016]. Thus, it seems possible that
645 KH waves at the magnetopause, especially at dusk, could drive field line resonances
646 throughout the dusk magnetosphere.
647
648 *Possible Sources of FLR: Planetary Period Oscillations*
649 Finally, as mentioned above, Yates et al. [2016] have presented high-latitude
650 observations of ~1-hour periodicities in the magnetic field, primarily transverse to the
651 average field. They have identified these fluctuations as second harmonic Alfvén waves
652 standing on closed outer-magnetospheric field lines. The fluctuations analyzed by Yates
653 et al. persisted for 6 days, from day 338 (4 Dec) through day 343 (9 Dec) of 2006. From
654 Table 2 we note that one of the banded-ion events we have found occurred on the day
655 preceding the Yates interval, while Cassini was outbound through the inner

656 magnetosphere. This close proximity in time provides yet another link between banded
657 ions and FLRs. Further, the long duration of the Yates interval suggests that stimulation
658 of the waves by a passing solar wind dynamic pressure enhancement is unlikely.
659 Most intriguingly, Yates et al. [2016] found that the 1-hour magnetic fluctuations
660 were temporally modulated, occurring in wave packets that in the northern hemisphere
661 recur periodically at the northern magnetic oscillation period [e.g., Gurnett et al., 2009;
662 Andrews et al., 2012; Provan et al., 2012]. They attributed the wave packet structure to a
663 rocking of the magnetosphere due to whatever dynamical process is responsible for the
664 much-studied planetary period oscillations (PPO) (see Carbary and Mitchell [2013] for a
665 review of PPO observations and models and Cowley et al. [2016a] for a recent update).
666 As for the source of the Alfvén waves themselves, Yates et al. [2016] suggested that they
667 "are probably generated by some dynamical process occurring in the outer
668 magnetosphere or in the central plasma sheet".
669 The PPOs observed in magnetic field measurements have been very successfully
670 modeled by a dual corotating field-aligned current system [e.g., Southwood and
671 Kivelson, 2007; Andrews et al., 2010, 2012; Provan et al., 2012; Cowley et al., 2016b].
672 These field-aligned currents emerge naturally from the atmospheric vortex model of
673 PPOs, which imposes a rotating pattern of flow in the ionosphere that results in periodic
674 modulation of the magnetosphere-ionosphere coupling currents [Jia et al., 2012; Jia and
675 Kivelson, 2012]. While it is well beyond the scope of this paper to investigate the
676 possibility, we offer the speculation that it may be these time-varying field-aligned
677 currents associated with the planetary period oscillations that periodically power the
678 Alfvén waves that form the field line resonances in the magnetosphere. Kivelson and Jia

679 [2014] showed how compressional fronts are launched by these ionospheric current
680 sources of planetary period oscillations. Since any compressional disturbance has the
681 possibility of coupling into a field line resonance, generation of FLRs might be a nearly
682 continuous process, modulated at the planetary period.

683 Such an internal source would account for the wide distribution of ~1-hour
684 periodic phenomena throughout Saturn's magnetosphere. In particular, field line
685 resonances would not be confined to the outer magnetosphere, but could potentially be
686 produced in the inner magnetosphere where we observe the banded ions. Moreover,
687 FLRs would be expected to be a rather common occurrence throughout the
688 magnetosphere, not requiring the relatively infrequent dynamic pressure events in the
689 solar wind, nor any particular KH activity at the magnetopause. Indeed, as pointed out
690 above, the Yates et al. observations showed the 1-h waves persisting for at least 6 days,
691 which is quite unlikely for FLRs created by a single solar wind pressure pulse. Further,
692 this would require relatively stable solar wind properties over that time scale if Kelvin-
693 Helmholtz waves are to be the source, but such long intervals would easily be consistent
694 with a repeating internal source.
695
696 Summary
697 1. On 3 May 2005 (day 123) the cool ion distribution observed by Cassini exhibited
698 ~3-4 discrete bands in E/q. The band energies uniformly decreased with
699 increasing radial distance, but they appeared superimposed on a background
700 thermal population that followed the expected general increase with r.

2. The banded ions were a globally coherent feature, lasting at least ~4 hours, and covering at least the L range from 5.7 to 7.5, the local time region from pre-midnight to ~2 LT, and ~106˚ of SLS2 longitude [e.g., Kurth et al., 2007].
3. The fact that the energy flux was larger for particles coming from the equator than for particles coming from high latitudes points to a more equatorial source of the population or possibly one in the southern hemisphere.
4. The energy of the bands appeared to decrease with increasing pitch angle, even across 90˚.
5. The bands that CAPS saw were dominantly H^+, and we are unable to determine whether or not the heavier species (H_2^+ and W^+) were similarly banded, preventing the type of species comparisons (e.g., common energy or common time of flight) that have proven valuable at Earth [e.g., Colpitts et al., 2016].
6. Projecting backwards in time, the banded ions seen by Cassini would have departed the equator in the premidnight region ~0.5-1.5 hours prior to their observation (the shorter travel times corresponding to the higher-energy bands). The times between the projected departures of the various energy bands would have been ~1000-2000 s, comparable to the estimated half bounce period of Alfvén waves on these field lines. Departure from a southern magnetic latitude of 20˚ rather than the equator would have resulted in roughly twice that travel time and twice the difference times, but again the difference times would be comparable to the Alfvén wave half bounce period.
7. We hypothesize that the banded ions are formed by a bounce-resonant interaction between magnetospheric H^+ ions and the standing wave structure of a field-line

resonance. The observed band energies are consistent with the expectation that the bounce period of resonant particles would be related to the Alfvén bounce period by Equation 4. For the plasma and field parameters we have adopted for the calculation, the n=1 FLR (with a peak wave amplitude near the equator) seems to provide a better match to the band energies in that it allows a frequency match for relatively low orders of the bounce resonance (m=1,2,…), but with reasonable variations of the plasma and field properties, the n=2 FLR might also give a satisfactory match.

8. The pitch-angle dependence of the band energies is generally consistent with the bounce resonance hypothesis, except that the band energies decrease rather than increase with pitch angle above 90˚. This feature is robust throughout much of the interval of the bands. It may indicate that these particles, which are traveling away from the equatorial plane, have been less effectively accelerated during their interaction with the wave. Alternatively, we raise the possibility that the banded ions all encountered the wave most recently when and where it was at its most effective magnitude and direction for ion acceleration, so that they share a common time of flight from that region. This hypothesis reproduces well the pitch-angle dependence of the band energies, including the continued decrease across 90˚, especially if the effective acceleration region is taken to be at -20˚ latitude.
9. Estimates of the amplitude of flux modulation that might be expected from interaction of magnetospheric plasma with FLRs are plausibly in range of the observed flux variations in the bands.

10. One possible source of such FLRs is the coupling of a fast-mode compressional wave propagating through the inner magnetosphere, perhaps as the magnetospheric response to a sudden solar wind dynamic pressure enhancement. However, we find no evidence in the magnetic field or SKR observations to support the occurrence of such a large-scale compression in the required time frame, although we do find possible evidence for the magnetic fluctuations arising from a field line resonance.
11. Other possible FLR sources might be Kelvin-Helmholtz waves generated at the magnetopause or possibly the variable field-aligned current system and compressional disturbances associated with planetary period oscillations.

Conclusion

While energy-banded ions are observed not uncommonly in Earth's magnetosphere, we have reported here the first observation of banded ions at Saturn. Observed near midnight at relatively high magnetic latitudes within the inner magnetosphere, the banded ions are dominantly H+, and they occupy the range of energies typically associated with the thermal pick-up distribution in the inner magnetosphere. The observed energies of the bands, including their pitch angle variation, are consistent with a bounce-resonant interaction between thermal H^+ ions and the standing wave structure of a field line resonance. There is evidence in the pitch-angle dependence of the band energies that the particles in each band may have a common time of flight from their most recent interaction with the wave, which may have been at slightly southern latitudes. While it is beyond the scope of this paper to determine

definitively the process(es) producing these energy bands, we hope that it will stimulate further attention to mechanisms of thermal ion acceleration in Saturn's magnetosphere, as well as studies of field line resonances there.

Acknowledgements

This work benefited greatly from collaborative discussions that took place during a visit of MFT to the University of Southampton as a Diamond Jubilee fellow. The support provided by the Diamond Jubilee Fellowship is gratefully acknowledged. Work at PSI was supported by the NASA Cassini program through JPL contract 1243218 with Southwest Research Institute. The Cassini project is managed by the Jet Propulsion Laboratory for NASA. SVB is supported by STFC Ernest Rutherford Fellowship ST/M005534/1. CMJ is supported by a Science and Technology Facilities Council Ernest Rutherford Fellowship ST/L004399/1. MGK is supported by NASA grant NNX14AG87G:000002. The research at the University of Iowa was supported by NASA through Contract 1415150 with the Jet Propulsion Laboratory. Work by XJ is supported by NASA grant NNX15AH28G. All Cassini plasma, magnetometer, and plasma wave data used for this study are available from the Planetary Data System (http://pds.nasa.gov/). We thank K.C. Hansen and B. Zieger for providing solar wind propagations from their Michigan Solar Wind Model (http://mswim.engin.umich.edu/).

References

793 Anderson, B. J., Potemra, T. A., Zanetti, L. J., and Engebretson, M. J. (1991), Statistical
794 correlations between Pc3–5 pulsations and solar wind/IMF parameters and
795 geomagnetic indices, in *Physics of Space Plasmas (1990),* SPI Conf. Proc. Reprint
796 Ser., 10, edited by T. Chang et al., 419–429, Scientific, Cambridge, Mass.
797 Andrews, D. J., A. J. Coates, S. W. H. Cowley, M. K. Dougherty, L. Lamy, G. Provan,
798 and P. Zarka (2010), Magnetospheric period oscillations at Saturn: Comparison of
799 equatorial and high latitude magnetic field periods with north and south Saturn
800 kilometric radiation periods, *J. Geophys. Res., 115,* A12252,
801 doi:10.1029/2010JA015666.
802 Andrews, D. J., S. W. H. Cowley, M. K. Dougherty, L. Lamy, G. Provan, and D. J.
803 Southwood (2012), Planetary period oscillations in Saturn's magnetosphere:
804 Evolution of magnetic oscillation properties from southern summer to post-equinox,
805 *J. Geophys. Res., 117*, A04224, doi:10.1029/2011JA017444.
806 Borodkova, N., et al. (2005), Large and sharp solar wind dynamic pressure variations as a
807 source of geomagnetic field disturbances at the geosynchronous orbit, *Plan. Space*
808 *Sci., 53,* 25-32, doi:10.1016/j.pss.2004.09.025.
809 Bridge, H. S., et al. (1981), Plasma observations near Saturn – initial results from
810 Voyager-1, *Science, 212,* 217-224, doi:10.1126/science.212.4491.217.
811 Bunce, E. J., S. W. H. Cowley, D. M. Wright, A. J. Coates, M. K. Dougherty, N. Krupp,
812 W. S. Kurth, and A. M. Rymer (2005), In situ observations of a solar wind
813 compression-induced hot plasma injection in Saturn's tail, *Geophys. Res. Lett., 32*,
814 L20S04, doi:10.1029/2005GL022888.

815 Burch, J. L., J. Goldstein, T. W. Hill, D. T. Young, F. J. Crary, A. J. Coates, N. André,
816 W. S. Kurth, and E. C. Sittler Jr. (2005), Properties of local plasma injections in
817 Saturn's magnetosphere, *Geophys. Res. Lett., 32*, L14S02,
818 doi:10.1029/2005GL022611.
819 Burton, M. E., M. K. Dougherty, and C. T. Russell (2010), Saturn's internal planetary
820 magnetic field, *Geophys. Res. Lett., 37,* L24105, doi:10.1029/2010GL045148.
821 Carbary, J. F., and D. G. Mitchell (2013), Periodicities in Saturn's magnetosphere, *Rev.*
822 *Geophys.,* 51, 1–30, doi:10.1002/rog.20006.
823 Chen, L., and A. Hasegawa (1974), A theory of long-period magnetic pulsations: 1.
824 Steady state excitation of field line resonance, *J. Geophys. Res., 79*(7), 1024–1032,
825 doi:10.1029/JA079i007p01024.
826 Chi, P. J., D.-H. Lee, and C. T. Russell (2006), Tamao travel time of sudden impulses and
827 its relationship to ionospheric convection vortices, *J. Geophys. Res., 111*, A08205,
828 doi:10.1029/2005JA011578.
829 Colpitts, C. A., C. A. Cattell, J. U. Kozyra, M. F. Thomsen, and B. Lavraud (2016),
830 Satellite observations of energy-banded ions during large geomagnetic storms: Event
831 studies, statistics, and comparisons to source models, *J. Geophys. Res., 121,* 6353–
832 6377, doi:10.1002/2016JA022481.
833 Cowley, S. W. H., P. Zarka, G. Provan, L. Lamy, and D. J. Andrews (2016a), Comment
834 on "A new approach to Saturn's periodicities" by J. F. Carbary, *J. Geophys. Res.,*
835 *121,* 2418, doi:10.1002/2015JA021996.
836 Cowley, S. W. H., G. Provan, G. J. Hunt, and C. M. Jackman (2016b), Planetary period
837 modulations of Saturn's magnetotail current sheet: A simple illustrative mathematical

838 model, *J. Geophys. Res., 121*, doi: 10.1002/2016JA023367.
839 Cutler, J. C., M.K. Dougherty, E.A. Lucek, A. Masters (2011), Evidence of surface wave
840 on the dusk flank of Saturn's magnetopause possibly caused by the Kelvin–Helmholtz
841 instability, *J. Geophys. Res., 116,* A10220, doi:10.1029/2011JA016643.
842 Delamere, P. A., R. J. Wilson, S. Eriksson, and F. Bagenal (2013), Magnetic signatures
843 of Kelvin-Helmholtz vortices on Saturn's magnetopause: Global survey, *J. Geophys.*
844 *Res., 118,* 393, doi: 10.1029/2012JA018197.
845 Desch, M. D. (1982), Evidence for solar wind control of Saturn radio emission, *J.*
846 *Geophys. Res., 87*(A6), 4549–4554, doi:10.1029/JA087iA06p04549.
847 Desroche, M., F. Bagenal, P. A. Delamere, and N. Erkaev (2013), Conditions at the
848 magnetopause of Saturn and implications for the solar wind interaction, *J. Geophys.*
849 *Res., 118,* 3087, doi: 10.1002/jgra.50294.
850 Dougherty, M. K., et al. (2004), The Cassini magnetic field investigation, *Space Sci.*
851 *Rev., 114,* 331-383.
852 Engebretson, M. J., Glassmeier, K.-H., and Stellmacher, M. (1998), The dependence of
853 high-latitude Pc5 power on solar wind velocity and phase of high-speed solar wind
854 streams, *J. Geophys. Res., 103*, 26271–26283.
855 Galopeau, P., P. Zarka, and D. Le Quéau (1989), Theoretical model of Saturn's kilometric
856 radiation spectrum, *J. Geophys. Res., 94*(A7), 8739–8755,
857 doi:10.1029/JA094iA07p08739.
858 Grodent, D., J. Gustin, J. C. Gerard, A. Radioti, B. Bonfond, and W. R. Pryor (2011),
859 Small-scale structures in Saturn's ultraviolet aurora, *J. Geophys. Res., 116,* A09225,
860 doi: 10.1029/2011JA016818.

861 Gurnett, D. A., et al. (2004), The Cassini radio and plasma wave investigation, *Space Sci.*
862 *Rev., 114,* 395-463.
863 Gurnett, D. A., A. Lecacheux, W. S. Kurth, A. M. Persoon, J. B. Groene, L. Lamy, P.
864 Zarka, and J. F. Carbary (2009), Discovery of a north-south asymmetry in Saturn's
865 radio rotation period, *Geophys. Res. Lett., 36,* L16102, doi:10.1029/2009GL039621.
866 Gurnett, D. A., J. B. Groene, T. F. Averkamp, W. S. Kurth, S.-Y. Ye, and G. Fischer
867 (2011), The SLS4 longitude system based on a tracking filter analysis of the
868 rotational modulation of Saturn kilometric radiation, in *Planetary Radio Emissions*
869 *VII*, edited by H. O. Rucker, W. S. Kurth, P. Louarn, and G. Fischer, pp. 51–64,
870 Austrian Acad. Sci. Press, Vienna.
871 Hill, T. W., A. M. Rymer, J. L. Burch, F. J. Crary, D. T. Young, M. F. Thomsen, D.
872 Delapp, N. André, A. J. Coates, and G. R. Lewis (2005), Evidence for rotationally
873 driven plasma transport in Saturn's magnetosphere, *Geophys. Res. Lett., 32*, L14S10,
874 doi:10.1029/2005GL022620.
875 Holmberg, M. K. G., J.-E. Wahlund, M. W. Morooka, and A. M. Persoon (2012), Ion
876 densities and velocities in the inner plasma torus of Saturn, *Plan. Space Sci., 73,* 151,
877 doi:10.1016/j.pss.2012.09.016.
878 Hughes, W. J. (1994), Magnetospheric, ULF waves: A tutorial with a historical
879 perspective, in Solar Wind Sources of Magnetospheric Ultra-Low-Frequency Waves,
880 pp. 1–11, AGU, Washington, D. C.
881 Jackel, B. J., B. McKiernan, and H. J. Singer (2012), Geostationary magnetic field
882 response to solar wind pressure variations: Time delay and local time variation, *J.*
883 *Geophys. Res., 117*, A05203, doi:10.1029/2011JA017210.

884 Jackman, C. M., L. Lamy, M. P. Freeman, P. Zarka, B. Cecconi, W. S. Kurth, S. W. H.
885 Cowley, and M. K. Dougherty (2009), On the character and distribution of lower-
886 frequency radio emissions at Saturn and their relationship to substorm-like events, *J.*
887 *Geophys. Res., 114,* A08211, doi:10.1029/2008JA013997.
888 Jackman, C. M., C. S. Arridge, J. A. Slavin, S. E. Milan, L. Lamy, M. K. Dougherty, and
889 A. J. Coates (2010), In situ observations of the effect of a solar wind compression on
890 Saturn's magnetotail, *J. Geophys. Res., 115*, A10240, doi:10.1029/2010JA015312.
891 Jia, X., and M. G. Kivelson (2012), Driving Saturn's magnetospheric periodicities from
892 the upper atmosphere/ ionosphere: Magnetotail response to dual sources, *J. Geophys.*
893 *Res., 117*, A11219, doi:10.1029/2012JA018183.
894 Jia, X., K. C. Hansen, T. I. Gombosi, M. G. Kivelson, G. Tóth, D. L. DeZeeuw, and A. J.
895 Ridley (2012), Magnetospheric configuration and dynamics of Saturn's
896 magnetosphere: A global MHD simulation, *J. Geophys. Res., 117*, A05225,
897 doi:10.1029/2012JA017575.
898 Kivelson, M. G., and D. J. Southwood (1985), Resonant ULF waves: A new
899 interpretation, *Geophys. Res. Lett., 12*, 49, doi: 10.1029/GL012i001p00049.
900 Kivelson, M. G., and D. J. Southwood (1991), Ionospheric traveling vortex generation by
901 solar wind buffeting of the magnetosphere, *J. Geophys. Res., 96*(A2), 1661–1667,
902 doi:10.1029/90JA01805.
903 Kurth, W. S., G. B. Hospodarsky, D. A. Gurnett, B. Cecconi, P. Louarn, A. Lecacheux, P.
904 Zarka, H. O. Rucker, M. Boudjada, and M. L. Kaiser (2005), High spectral and
905 temporal resolution observations of Saturn kilometric radiation, *Geophys. Res. Lett.,*
906 *32*, L20S07, doi:10.1029/2005GL022648.

907 Kurth, W. S., A. Lecacheux, T. F. Averkamp, J. B. Groene, and D. A. Gurnett (2007), A
908 Saturnian longitude system based on a variable kilometric radiation period, *Geophys.*
909 *Res. Lett., 34,* L02201, doi:10.1029/2006GL028336.
910 Lamy, L., P. Zarka, B. Cecconi, S. Hess, and R. Prangé (2008), Modeling of Saturn
911 kilometric radiation arcs and equatorial shadow zone, *J. Geophys. Res., 113*, A10213,
912 doi:10.1029/2008JA013464.
913 Le, G., et al. (2004), Coordinated polar spacecraft, geosynchronous spacecraft, and
914 ground-based observations of magnetopause processes and their coupling to the
915 ionosphere, *Ann. Geophys., 22,* 4329-4350, doi:10.5194/angeo-22-4329-2004.
916 Leisner, J. S., C. T. Russell, M. K. Dougherty, X. Blanco-Cano, R. J. Strangeway, and C.
917 Bertucci (2006), Ion cyclotron waves in Saturn's E ring: Initial Cassini observations,
918 *Geophys. Res. Lett., 33*, L11101, doi:10.1029/2005GL024875.
919 Livi, R., J. Goldstein, J. L. Burch, F. Crary, A. M. Rymer, D. G. Mitchell, and A. M.
920 Persoon (2014), Multi-instrument analysis of plasma parameters in Saturn's
921 equatorial, inner magnetosphere using corrections for spacecraft potential and
922 penetrating background radiation, *J. Geophys. Res., 119,* 3683,
923 DOI:10.1002/2013JA019616.
924 Lysak, R. L., and D. H. Lee (1992), Response of the dipole magnetosphere to pressure
925 pulses, *Geophys. Res. Lett., 19,* 937-940, doi:10.1029/92GL00625.
926 Masters, A., N. Achilleos, C. Bertucci, M.K. Dougherty, S.J. Kanani, C.S. Arridge, H.J.
927 McAndrews, and A.J. Coates (2009), Surface waves on Saturn's dawn flank
928 magnetopause driven by the Kelvin–Helmholtz instability, *Plan. Space Sci., 57,* 1769.

929 Masters, A., N. Achilleos, M.G. Kivelson, N. Sergis, M.K. Dougherty, M.F. Thomsen,
930 C.S. Arridge, S.M. Krimigis, H.J. McAndrews, S.J. Kanani, N. Krupp, and A.J.
931 Coates (2010), Cassini observations of a Kelvin–Helmholtz vortex in Saturn's outer
932 magnetosphere, *J. Geophys. Res., 115*, A07225, doi:10.1029/2010JA015351.
933 Masters, A., N. Achilleos, J. C. Cutler, A. J. Coates, M. K. Dougherty, and G. H. Jones
934 (2012), Surface waves on Saturn's magnetopause, *Plan. Space Sci., 65,* 109, doi:
935 10.1016/j.pss.2012.02.007.
936 Mitchell, D. G., et al. (2005), Energetic ion acceleration in Saturn's magnetotail:
937 Substorms at Saturn? *Geophys. Res. Lett., 32,* L20S01, doi:10.1029/2005GL022647.
938 Mitchell, D. G., J. F. Carbary, E. J. Bunce, A. Radioti, S. V. Badman, W. R. Pryor, G. B.
939 Hospodarsky, and W. S. Kurth, Recurrent pulsations in Saturn's high latitude
940 magnetosphere, *Icarus, 263,* 94, doi: 10.1016/j.icarus.2014.10.028.
941 Palmaerts, B., E. Roussos, N. Krupp, W. S. Kurth, D. G. Mitchell, and J. N. Yates (2016),
942 Statistical analysis and multi-instrument overview of the quasi-periodic 1-hour
943 pulsations in Saturn's outer magnetosphere, *Icarus, 271*, 1, doi:
944 10.1016/j.icarus.2016.01.025.
945 Porco, C. C., et al. (2006), Cassini observes the active south pole of Enceladus, *Science,*
946 *311,* 1393-1401, doi:10.1126/science.1123013.
947 Provan, G., D. J. Andrews, C. S. Arridge, A. J. Coates, S. W. H. Cowley, G. Cox, M. K.
948 Dougherty, and C. M. Jackman (2012), Dual periodicities in planetary-period
949 magnetic field oscillations in Saturn's tail, *J. Geophys. Res., 117*, A01209,
950 doi:10.1029/2011JA017104.

951 Rankin, R., C. Wang, D. Sydorenko, Y. Wang, Q.-G. Zong, and X. Zhou (2016),
952 Simulation of bounce-resonance ULF wave-particle interactions, 2016 URSI Asia-
953 Pacific Radio Sci. Conf. (URSI AP-RASC), pp. 956-959.
954 Ren, J., Q. G. Zong, X. Z. Zhou, R. Rankin, and Y. F. Wang (2016), Interaction of ULF
955 waves with different ion species: Pitch angle and phase space density implications, *J.*
956 *Geophys. Res. Space Physics, 121*, 9459–9472,doi:10.1002/2016JA022995.
957 Roussos, E., et al. (2016), Quasi-periodic injections of relativistic electrons in Saturn's
958 outer magnetosphere, *Icarus, 263,* 101, doi: 10.1016/j.icarus.2015.04.017.
959 Russell, C. T., J. S. Leisner, C. S. Arridge, M. K. Dougherty, and X. Blanco-Cano (2006),
960 Nature of magnetic fluctuations in Saturn's middle magnetosphere, *J. Geophys. Res.,*
961 *111*, A12205, doi:10.1029/2006JA011921.
962 Singer, H. J., C. T. Russell, M. G. Kivelson, E.W. Greenstadt, and J. V Olson (1977),
963 Evidence for the control of Pc3–4 magnetic pulsations by the solar wind velocity,
964 *Geophys. Res. Lett., 4,* 377–379.
965 Sittler, E. C., Jr., et al. (2005), Preliminary results on Saturn's inner plasmasphere as
966 observed by Cassini: Comparison with Voyager, *Geophys. Res. Lett., 32,* L14S07,
967 doi: 10.1029/2005GL022653.
968 Sittler, E. C., Jr., N. Andre, M. Blanc, M. Burger, R. E. Johnson, A. Coates, A. Rymer, D.
969 Reisenfeld, M. F. Thomsen, A. Persoon, M. Dougherty, H. T. Smith, R. A. Baragiola,
970 R. E. Hartle, D. Chornay, M. D. Shappirio, D. Simpson, D. J. McComas, and D. T.
971 Young (2008), Ion and neutral sources and sinks within Saturn's inner
972 magnetosphere: Cassini results, *Plan. Space Sci., 56*, 3.
973 Southwood, D. J. (1974), Some features of field line resonances in the magnetosphere,

974 *Plan. Space Sci., 22,* 483, doi:10.1016/0032-0633(74)90078-6.
975 Southwood, D. J., and M. G. Kivelson (1981), Charged particle behavior in low
976 frequency geomagnetic pulsations 1. Transverse waves, *J. Geophys. Res., 86,* 5643.
977 Southwood, D. J., and M. G. Kivelson (1982), Charged particle behavior in low
978 frequency geomagnetic pulsations 2. Graphical approach, *J. Geophys. Res., 87,* 1707.
979 Southwood, D. J., and M. G. Kivelson (1990), The magnetohydrodynamic response of
980 the magnetospheric cavity to changes in solar wind pressure, *J. Geophys. Res., 95,*
981 2301.
982 Southwood, D. J., and M. G. Kivelson (2007), Saturn magnetospheric dynamics:
983 Elucidation of a camshaft model, *J. Geophys. Res., 112*, A12222,
984 doi:10.1029/2007JA012254.
985 Tamao, T. (1964), A hydromagnetic interpretation of geomagnetic SSC*, *Rep. Ionos.*
986 *Space Res. Jpn., 18*, 16– 31.
987 Thomsen, M. F., and J. A. Van Allen (1980), Motion of trapped electrons and protons in
988 Saturn's inner magnetosphere, *J. Geophys. Res., 85,* 5831-5834.
989 Thomsen, M. F., D. B. Reisenfeld, D. M. Delapp, R. L. Tokar, D. T. Young, F. J. Crary,
990 E. C. Sittler, M. A. McGraw, and J. D. Williams (2010), Survey of ion plasma
991 parameters in Saturn's magnetosphere, *J. Geophys. Res., 115*, A10220,
992 doi:10.1029/2010JA015267.
993 Thomsen, M. F., et al. (2014), Ion composition in interchange injection events in Saturn's
994 magnetosphere, *J. Geophys. Res. Space Physics, 119*, 9761–9772,
995 doi:10.1002/2014JA020489.
996 Thomsen, M. F., C. M. Jackman, D. G. Mitchell, G. Hospodarsky, W. S. Kurth, and K. C.

997 Hansen (2015), Sustained lobe reconnection in Saturn's magnetotail, *J. Geophys. Res.*
998 *Space Physics, 120,* 10,257–10,274, doi:10.1002/2015JA021768.
999 Tokar, R. L., et al. (2008), Cassini detection of water-group pick-up ions in the Enceladus
1000 torus, *Geophys. Res. Lett., 35*, L14202, doi:10.1029/2008GL034749.
1001 Villante, U., and M. Piersanti (2008), An analysis of sudden impulses at geosynchronous
1002 orbit, *J. Geophys. Res., 113*, A08213, doi:10.1029/2008JA013028.
1003 Waite, J. H., et al. (2006), Cassini ion and neutral mass spectrometer: Enceladus plume
1004 composition and structure, *Science, 311,* 1419-1422, doi:10.1126/science.1121290.
1005 Wang, C., J. B. Liu, Z. H. Huang, and J. D. Richardson (2007), Response of the magnetic
1006 field in the geosynchronous orbit to solar wind dynamic pressure pulses, *J. Geophys.*
1007 *Res., 112,* A12210, doi:10.1029/2007JA012664.
1008 Wilson, R. J., R. L. Tokar, M. G. Henderson, T. W. Hill, M. F. Thomsen, and D. H.
1009 Pontius, Jr. (2008), Cassini plasma spectrometer thermal ion measurements in
1010 Saturn's inner magnetosphere, *J. Geophys. Res., 113*, A12218,
1011 doi:10.1029/2008JA013486.
1012 Wilson, R. J., R. L. Tokar, and M. G. Henderson (2009), Thermal ion flow in Saturn's
1013 inner magnetosphere measured by the Cassini plasma spectrometer: A signature of
1014 the Enceladus torus?, *Geophys. Res. Lett., 36,* L23104, doi:10.1029/2009GL040225.
1015 Wilson, R. J., P. A. Delamere, F. Bagenal, and A. Masters (2012), Kelvin-Helmholtz
1016 instability at Saturn's magnetopause: Cassini ion data analysis, *J. Geophys. Res., 117,*
1017 A03212, 10.1029/2011JA016723.
1018 Yang, B., Q.-G. Zong, Y. F. Wang, S. Y. Fu, P. Song, H. S. Fu, A. Korth, T. Tian, and H.
1019 Reme (2010), Cluster observations of simultaneous resonant interactions of ULF

waves with energetic electrons and thermal ion species in the inner magnetosphere, *J. Geophys. Res., 115,* A02214, doi:10.1029/2009JA014542.

Yang, B., Q.-G. Zong, S. Y. Fu, X. Li, A. Korth, H. S. Fu, C. Yue, and H. Reme (2011a), The role of ULF waves interacting with oxygen ions at the outer ring current during storm times, *J. Geophys. Res., 116,* A01203, doi:10.1029/2010JA015683.

Yang, B., et al. (2011b), Pitch angle evolutions of oxygen ions driven by storm time ULF poloidal standing waves, *J. Geophys. Res., 116*, A03207, doi:10.1029/2010JA016047.

Yates, J. N., et al. (2016), Saturn's quasiperiodic magnetohydrodynamic waves, *Geophys. Res. Lett., 43,* 11,102–11,111, doi:10.1002/2016GL071069.

Young, D. T., et al. (2004), Cassini Plasma Spectrometer investigation, *Space Sci. Rev., 114*, 1–112.

Young, D. T., et al. (2005), Composition and dynamics of plasma in Saturn's magnetosphere, *Science, 307,* 1262-1266, doi:10.1126/science.1106151.

Zieger, B., and K. C. Hansen (2008), Statistical validation of a solar wind propagation model from 1 to 10 AU, *J. Geophys. Res., 113,* A08107, doi:10.1029/2008JA013046.

Zong, Q.-G., Y. F. Wang, H. Zhang, S. Y. Fu, H. Zhang, C. R. Wang, C. J. Yuan, and I. Vogiatzis (2012), Fast acceleration of inner magnetospheric hydrogen and oxygen ions by shock induced ULF waves, *J. Geophys. Res., 117*, A11206, doi:10.1029/2012JA018024.

1041 Table 1. Exponential fits to Anode 1 band energies: $E=a\cdot\exp(-bx)$
1042

	Band 1	Band 2	Band 3
x=t			
a(eV)	316	631	1438
b(s^{-1})	-1.13×10^{-4}	-1.13×10^{-4}	-1.11×10^{-4}
R	0.980	0.991	0.982
x=L			
a(eV)	3426	7212	15755
b(R_s^{-1})	-0.885	-0.896	-0.881
R	0.981	0.991	0.982
x=λ			
a(eV)	1.60×10^{-3}	6.20×10^{-3}	1.67×10^{-2}
b(deg^{-1})	0.441	0.409	0.403
R	0.970	0.990	0.982

1043
1044

1045 Table 2. Other candidate banded-ion events
1046

Date	Time Range	Latitude	Local Time	L range	Notes
25 Jul 2006	0800-1110	11˚	18	7.8-9.4	Weak
9 Nov 2006	0630-0800	26˚	16	7.1-8.8	
3 Dec 2006	0430-0700	28˚	15	7.5-11	
24 Nov 2008	0400-0540	29˚	22	6.6-9.1	High telem rate

1047

1048 Figure Captions

1049 1. Color-coded count rate (proportional to energy flux) for ions observed by the
1050 Cassini/CAPS IMS on several passes through the inner magnetosphere: a) 16 Oct 2010;
1051 b) 9 Sep 2006; c) 21 May 2005; and d) 3 May 2005. Periodic structure seen in panels a
1052 and b is due to the actuation of the instrument, allowing the detectors to view different
1053 directions in space. CAPS was not actuating during the two intervals in panels c and d.
1054 The solid black line in each panel gives the local corotational energy of a proton. Panel d
1055 shows a set of discrete energy bands, with band energies that decrease with increasing
1056 radial distance. The spacecraft location in L, magnetic latitude (λ), and local time is
1057 indicated below the time axis.

1058 2. KSM (Kronocentric solar magnetospheric) X-Z and X-Y projections of Cassini orbits
1059 for the days shown in Figure 1. Each trajectory segment covers a full day (00-24 h).
1060 Heavy portions of each curve correspond to the actual time ranges from Figure 1. The
1061 sun is to the right of the figure. Plus markers on each curve do not indicate specific times
1062 (e.g., hours of the day), but are simply present to help identify the curves.

1063 3. Color-coded count rate spectrograms from four different CAPS/IMS anodes with
1064 different look directions for the 3 May 2005 interval shown in Figure 1d.

1065 4. Thirty-minute sum of counts in the TOF data product, sorted into species bins
1066 according to the procedure described in Thomsen et al. [2014]. Vertical bars span the
1067 range of energies of the first clear banded-ion peak in the SNG spectrum for all the
1068 anodes over this time range.

1069 5. a) Energy of the peak count rate in each of the ion bands seen in the four anodes
1070 shown in Figure 3, plotted versus time on 3 May 2005; b) same as Figure 5a for only

anode 1; c) same band energies from anode 1 plotted as a function of L, which increased monotonically with time during the interval; d) same band energies from anode 1 plotted as a function of magnetic latitude, which decreased monotonically during the interval. All band energies have been computed in the corotating frame of reference. The line in Figure 5a is the H+ corotation energy over the same time range. Lines in the other three panels are drawn to guide the eye in recognizing the discrete energy bands. Table 1 provides the coefficients of exponential fits to the three highlighted bands.

6. Five-minute accumulations of color-coded counts from SNG data, sorted into energy and pitch angle bins in the corotating frame: a) 0700-0705 UT, b) 0730-0735 UT, and c) 0800-0805 UT. Panels d, e, and f show the energy in the corotating frame of the identified bands at times corresponding to panels a, b, and c, respectively, plotted as a function of pitch angle in the corotating frame. For the spacecraft located at northern latitudes, pitch angles less than 90˚ correspond to particle moving southward toward the equator, whereas pitch angles greater than 90˚ correspond to particles moving northward away from the equator. Particles moving away from the equator show larger count rates and lower band energies than those moving toward it.

7. a) Quarter bounce period (i.e., travel time from the equator to the spacecraft) of locally mirroring band particles; b) time of day (in seconds) at which locally mirroring band particles would have had to leave the equator in order to arrive at the spacecraft at the observation time; c) local time at which locally mirroring band particles seen at Cassini would have left the equatorial plane, assuming full corotation; d) time separation between departure times of successive bands. For comparison, the solid curve shows one half of the bounce period of an Alfven wave, computed based on the densities and scale heights

1094 determined by Thomsen et al. [2010]. Band 1 corresponds to the lowest-energy band
1095 seen in the ion spectra.
1096 8. Bounce periods of locally mirroring protons at the observed band energies as a
1097 function of L, compared with harmonic multiples of the Alfvén wave bounce period, as
1098 expected for the fundamental mode of a field line resonance (left) and the first harmonic
1099 (right).
1100 9. Observed band energies (solid circles) as a function of local pitch angle at ~0700 UT,
1101 compared to calculated energies for which a) the bounce periods, b) the times of flight
1102 from the equator, or c) the times of flight from a latitude of -20˚ are equal to those for
1103 observed locally mirroring band particles.
1104 10. Same as Figure 7, except for a source location at -20˚ latitude.
1105 11. a) Magnetic field magnitude and azimuthal component observed by Cassini for the
1106 ten hours encompassing and preceding the banded ion observations. The solid bar above
1107 the upper panel indicates the range of backward-projected departure times of the lowest
1108 energy band of ions, both for an assumed equatorial source and for an assumed source at
1109 -20˚ latitude. If the initial energization of the ions were associated with a compressional
1110 wave propagating through the magnetosphere, its signature would presumably occur
1111 during this time interval. The dashed bar following the solid bar shows the time range
1112 over which subsequent field line resonances would be expected. The vertical bars in the
1113 B_ϕ panel indicate semi-periodic enhancements observed above the background B_ϕ. b)
1114 RPWS electric field spectra for 2-day intervals encompassing three consecutive periapsis
1115 passages by Cassini. The outbound passage on which the banded ions were observed is
1116 covered in the center panel. The time interval of the banded ion observation is indicated

1117 by the solid bars above and below that panel. c) Solar wind density, speed, and dynamic
1118 pressure at Saturn's location predicted by the mSWIM MHD model [Zieger and Hansen,
1119 2008] for a 50-d interval encompassing the three periapsis passes shown in Figure 11b
1120 (vertical dashed lines).
1121
1122
1123

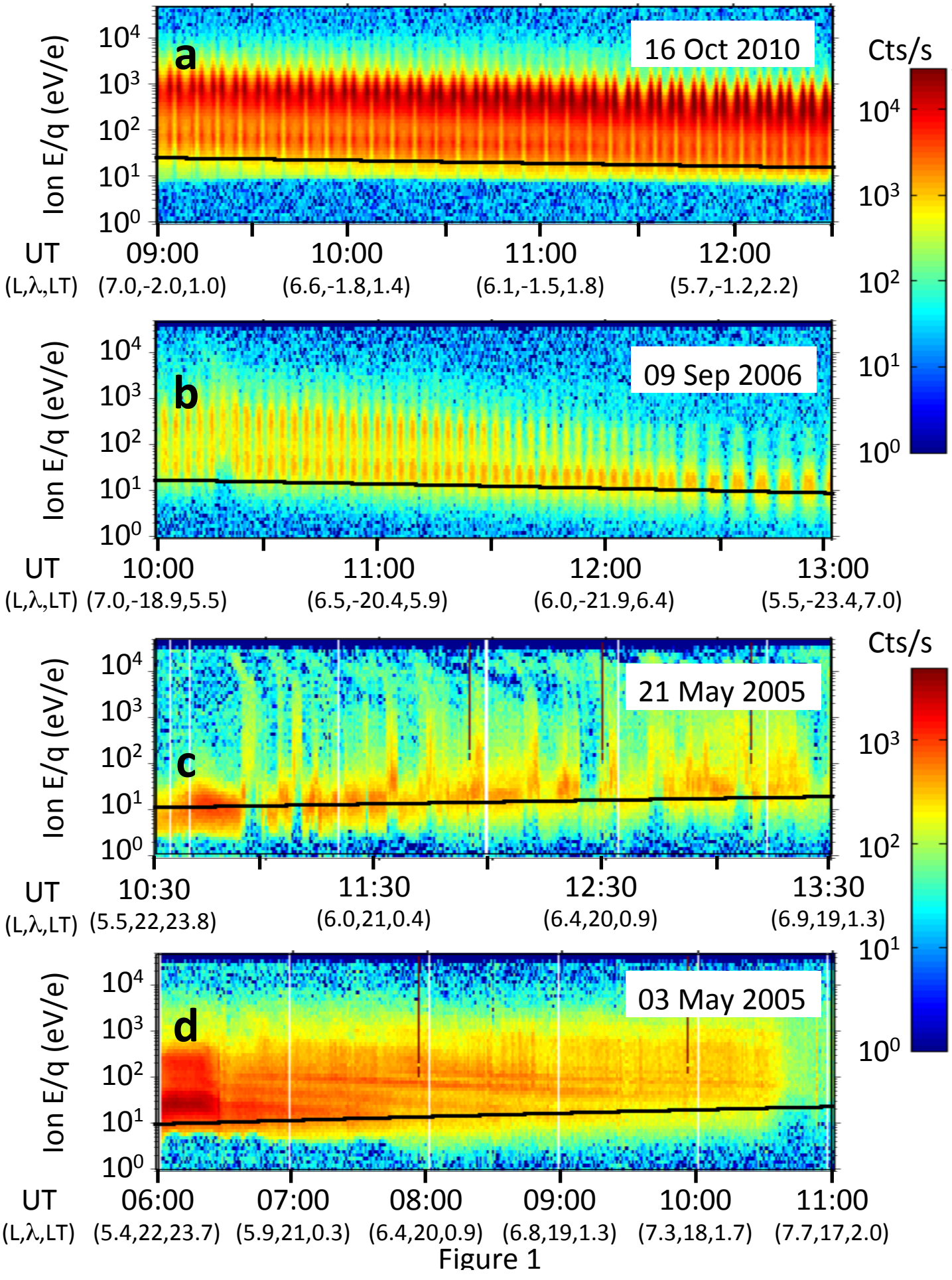
a
16 Oct 2010
Ion E/q (eV/e)
Cts/s
UT
(L,λ,LT)
09:00
(7.0,-2.0,1.0)
10:00
(6.6,-1.8,1.4)
11:00
(6.1,-1.5,1.8)
12:00
(5.7,-1.2,2.2)
b
09 Sep 2006
10:00
(7.0,-18.9,5.5)
11:00
(6.5,-20.4,5.9)
12:00
(6.0,-21.9,6.4)
13:00
(5.5,-23.4,7.0)
c
21 May 2005
10:30
(5.5,22,23.8)
11:30
(6.0,21,0.4)
12:30
(6.4,20,0.9)
13:30
(6.9,19,1.3)
d
03 May 2005
06:00
(5.4,22,23.7)
07:00
(5.9,21,0.3)
08:00
(6.4,20,0.9)
09:00
(6.8,19,1.3)
10:00
(7.3,18,1.7)
11:00
(7.7,17,2.0)

Figure 1

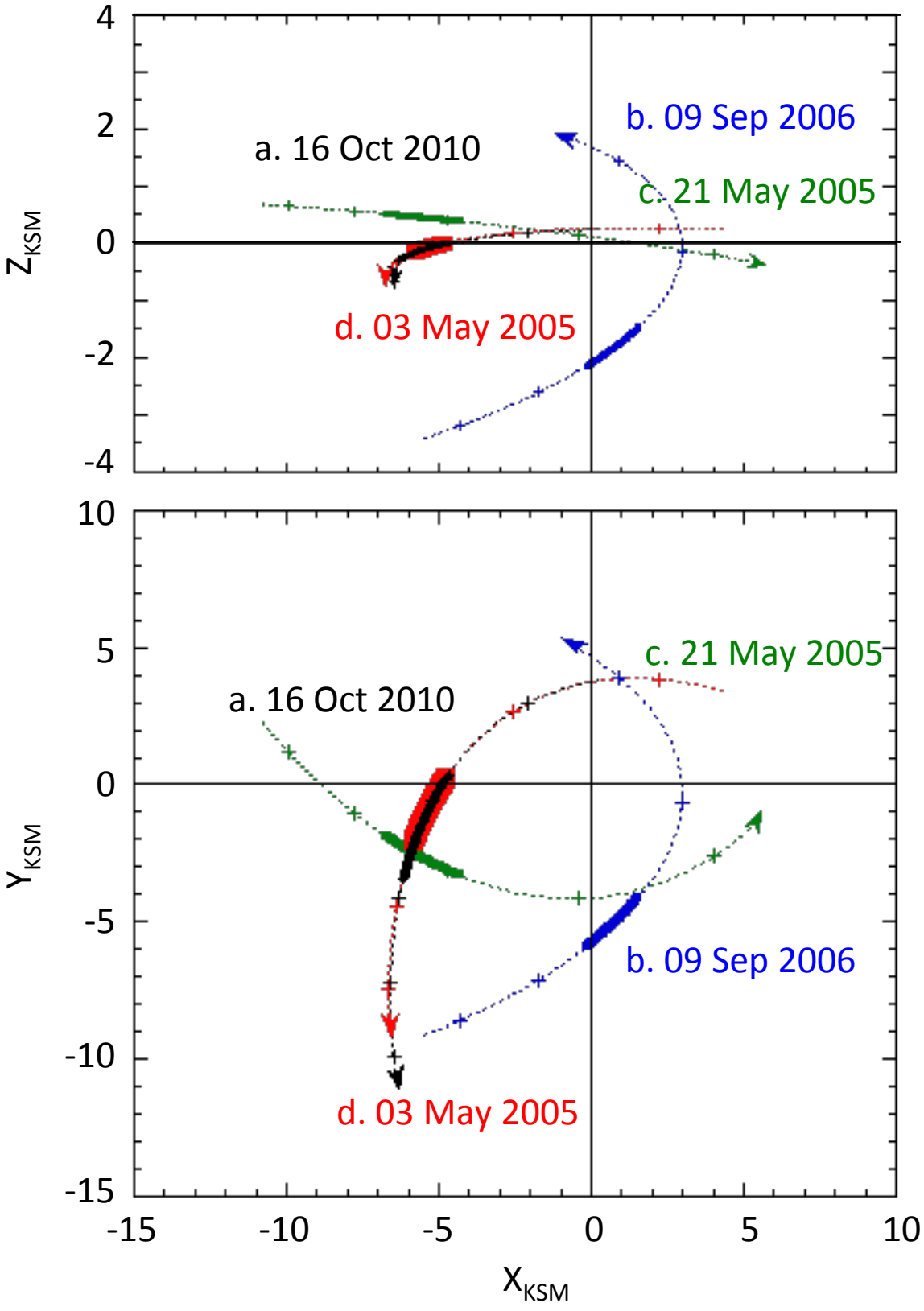
4
2
0
-2
-4
Z_{KSM}
a. 16 Oct 2010
b. 09 Sep 2006
c. 21 May 2005
d. 03 May 2005
10
5
0
-5
-10
-15
Y_{KSM}
a. 16 Oct 2010
c. 21 May 2005
b. 09 Sep 2006
d. 03 May 2005
-15
-10
-5
0
5
10
X_{KSM}

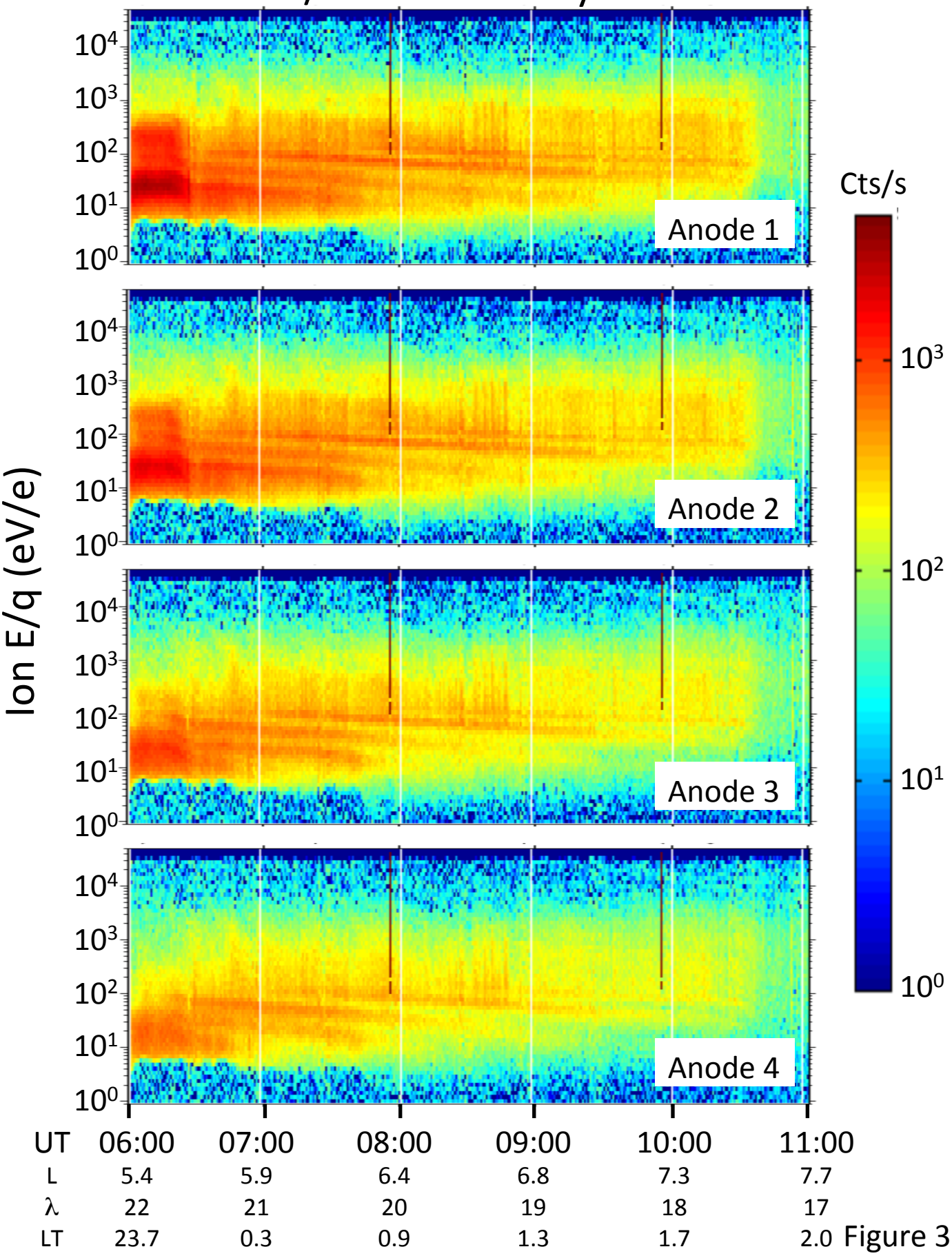
CAPS/IMS 03 May 2005
Ion E/q (eV/e)
10^4
10^3
10^2
10^1
10^0
Anode 1
Anode 2
Anode 3
Anode 4
Cts/s
10^3
10^2
10^1
10^0
UT 06:00 07:00 08:00 09:00 10:00 11:00
L 5.4 5.9 6.4 6.8 7.3 7.7
λ 22 21 20 19 18 17
LT 23.7 0.3 0.9 1.3 1.7 2.0

Figure 3

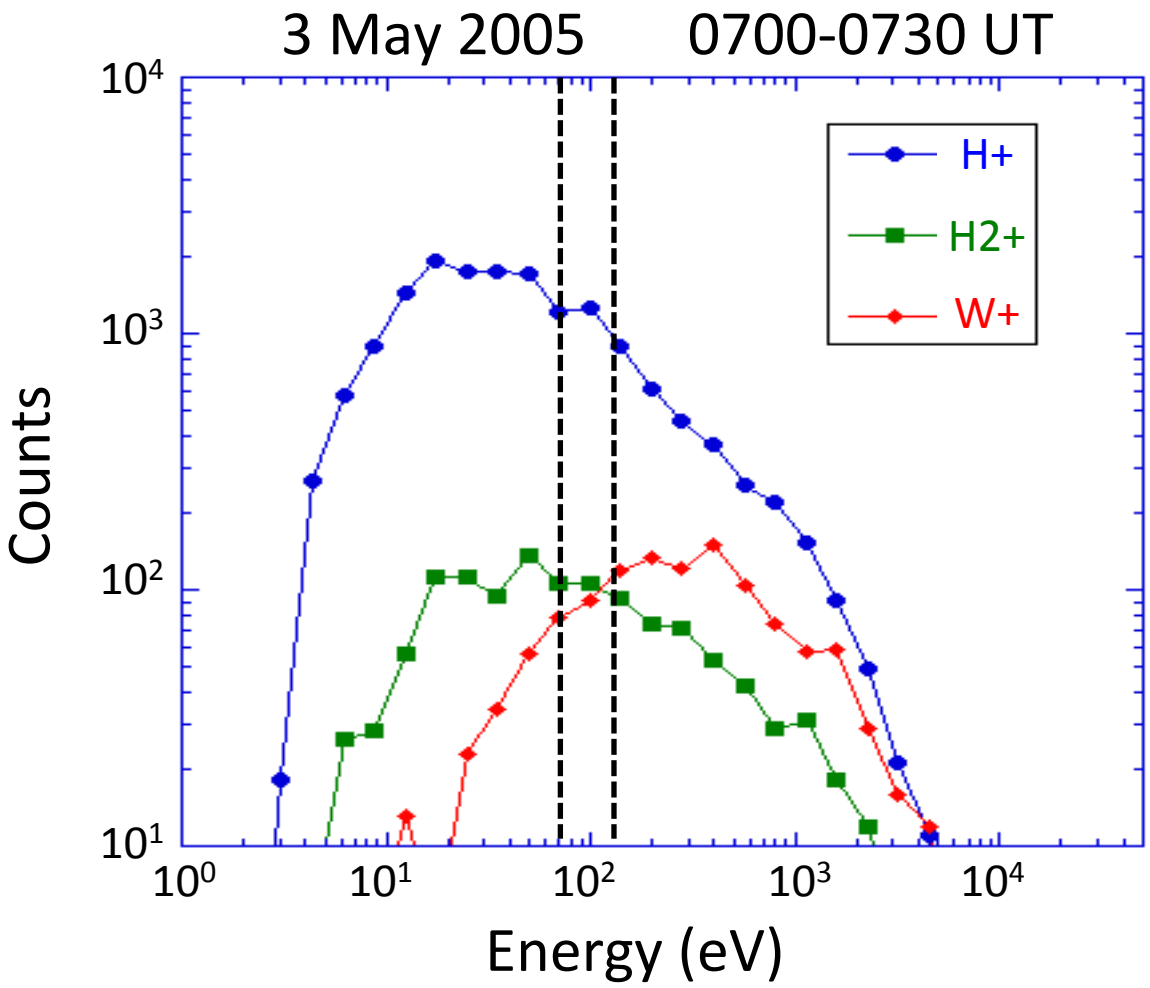
3 May 2005 0700-0730 UT
Counts
Energy (eV)
H+
H2+
W+
10^4
10^3
10^2
10^1
10^0
10^1
10^2
10^3
10^4

Figure 4

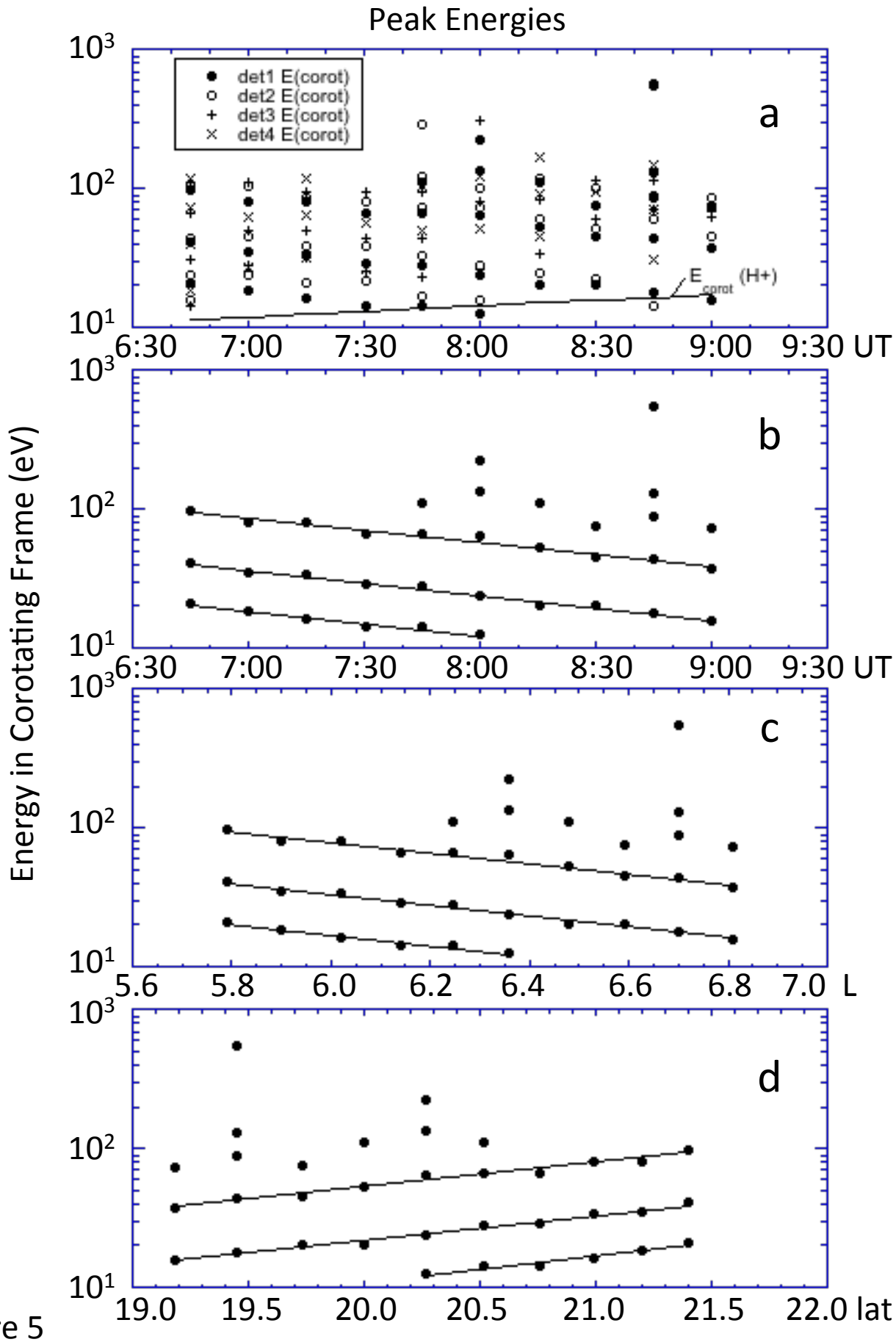
Peak Energies
det1 E(corot)
det2 E(corot)
det3 E(corot)
det4 E(corot)
a
E corot (H+)
b
c
d
Energy in Corotating Frame (eV)
6:30
7:00
7:30
8:00
8:30
9:00
9:30 UT
5.6
5.8
6.0
6.2
6.4
6.6
6.8
7.0 L
19.0
19.5
20.0
20.5
21.0
21.5
22.0 lat

Figure 5

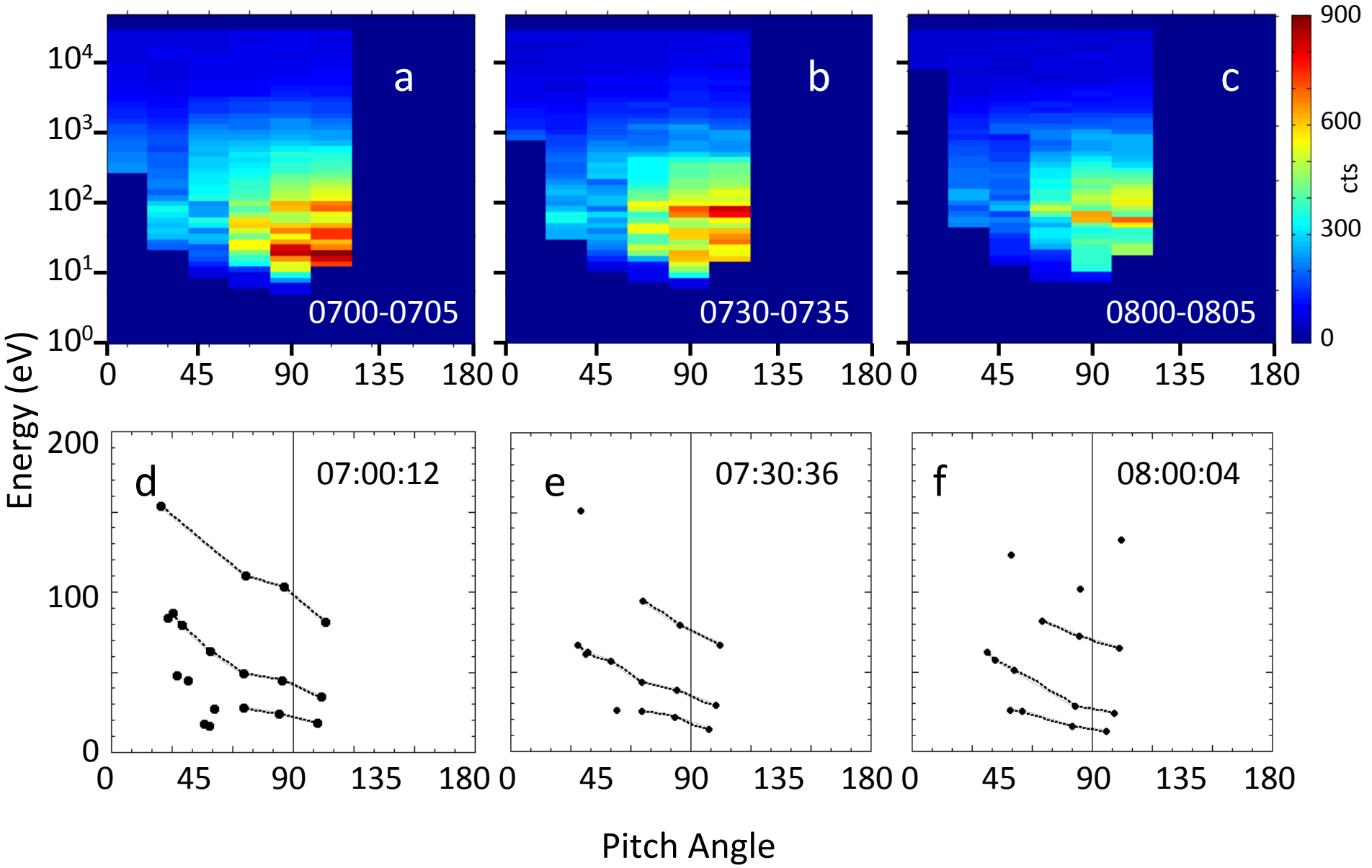
a
b
c
0700-0705
0730-0735
0800-0805
Energy (eV)
10^4
10^3
10^2
10^1
10^0
0
45
90
135
180
900
600
300
0
cts
d
e
f
07:00:12
07:30:36
08:00:04
200
100
0
Pitch Angle

Figure 6

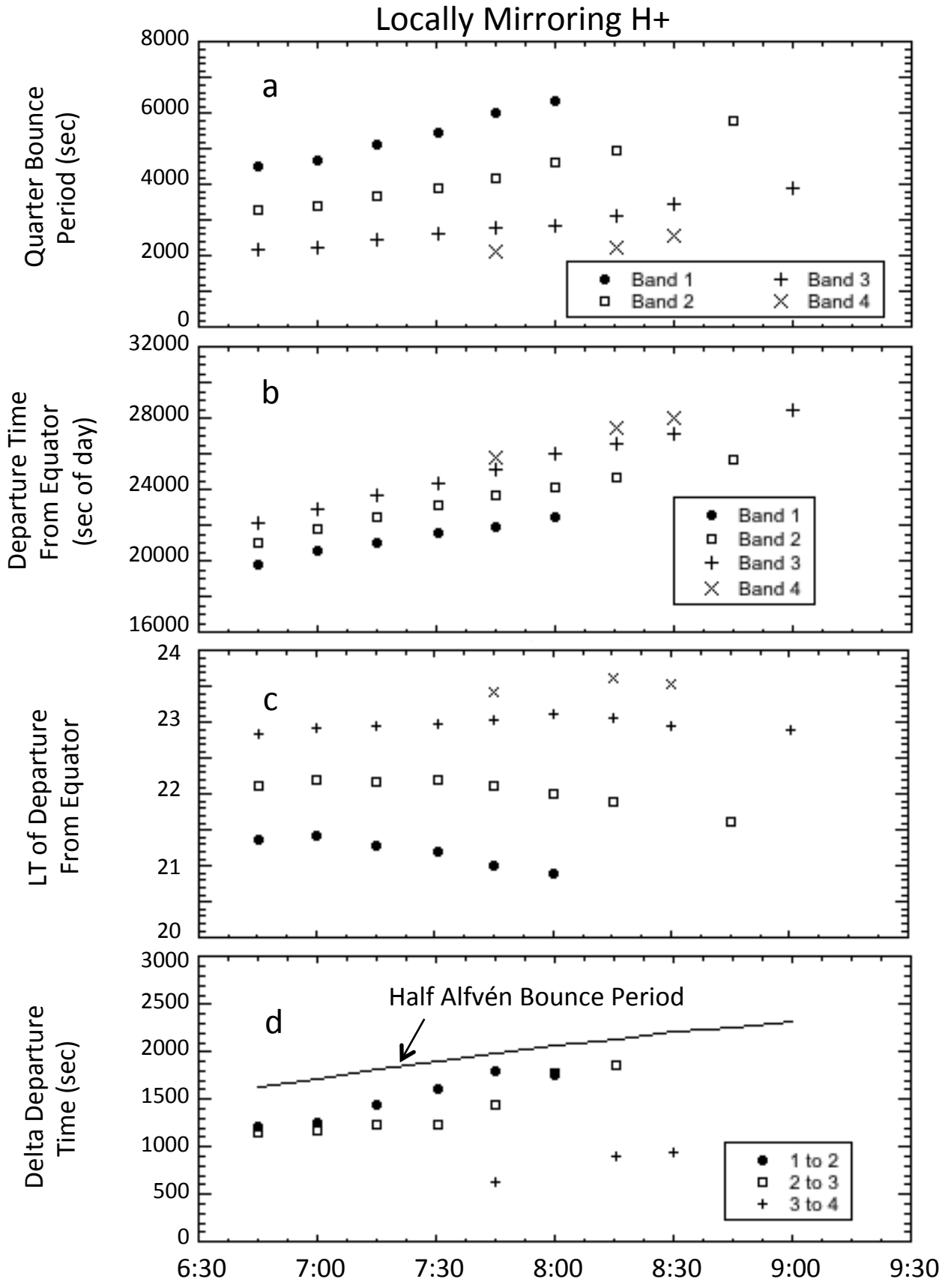
Locally Mirroring H+
Quarter Bounce Period (sec)
a
Band 1
Band 2
Band 3
Band 4
Departure Time From Equator (sec of day)
b
LT of Departure From Equator
c
Delta Departure Time (sec)
d
Half Alfvén Bounce Period
1 to 2
2 to 3
3 to 4
6:30
7:00
7:30
8:00
8:30
9:00
9:30
UT, 3 May 2005

Figure 7

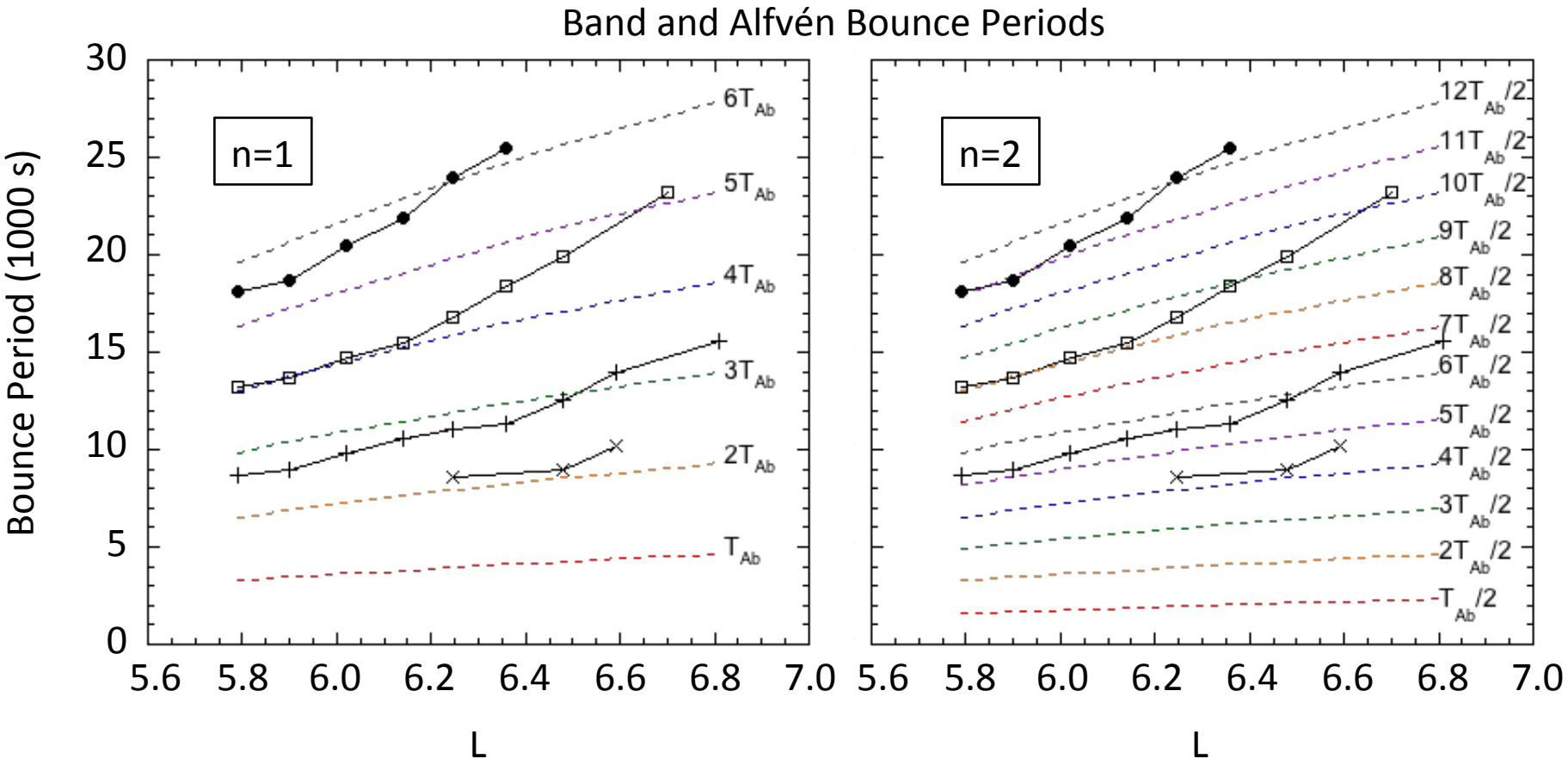
Band and Alfvén Bounce Periods
Bounce Period (1000 s)
30
25
20
15
10
5
0
n=1
6T Ab
5T Ab
4T Ab
3T Ab
2T Ab
T Ab
5.6
5.8
6.0
6.2
6.4
6.6
6.8
7.0
L
n=2
12T Ab/2
11T Ab/2
10T Ab/2
9T Ab/2
8T Ab/2
7T Ab/2
6T Ab/2
5T Ab/2
4T Ab/2
3T Ab/2
2T Ab/2
T Ab/2
5.6
5.8
6.0
6.2
6.4
6.6
6.8
7.0
L

Figure 8

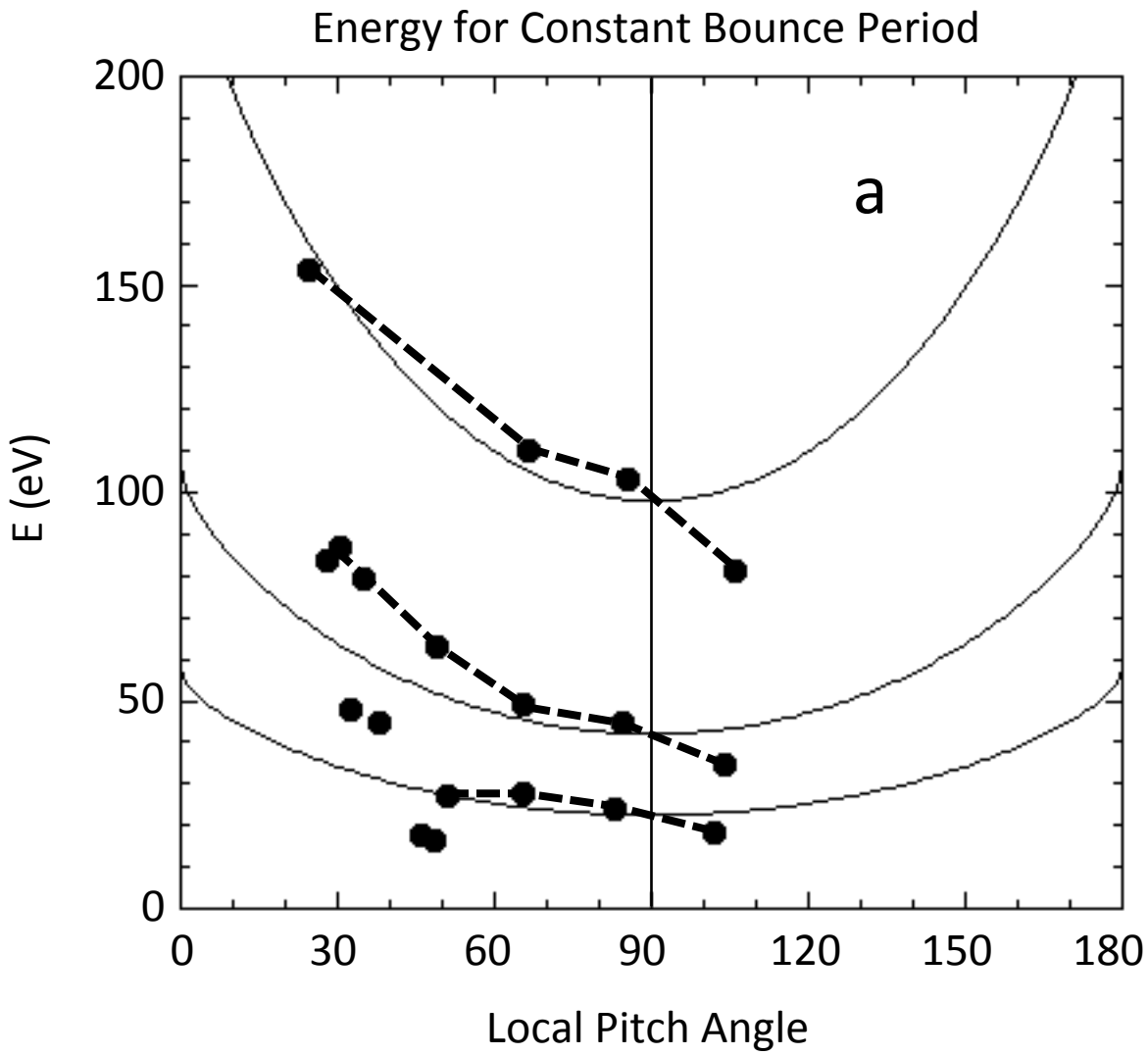
Energy for Constant Bounce Period
a
E (eV)
200
150
100
50
0
0
30
60
90
120
150
180
Local Pitch Angle

Figure 9a

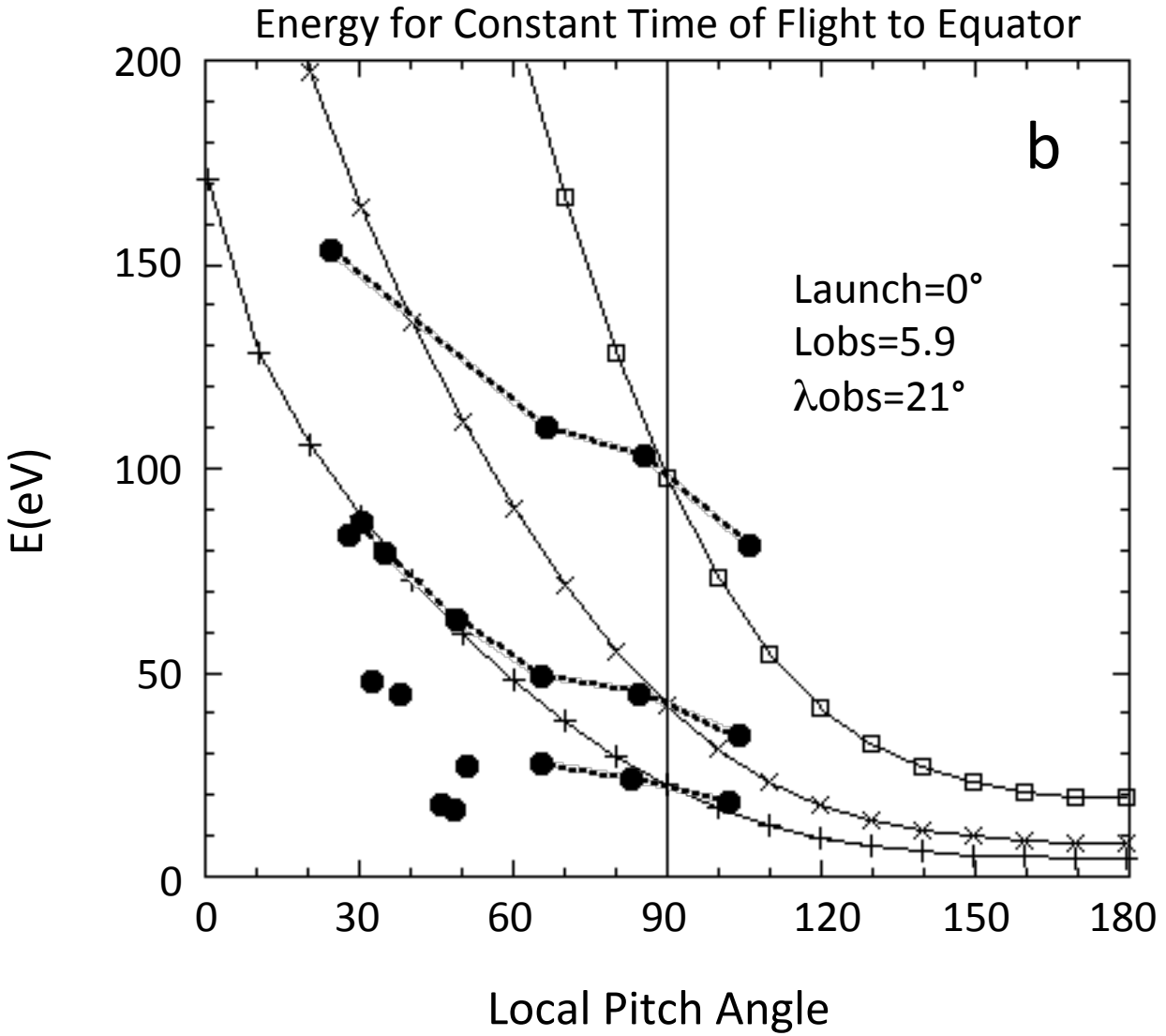
Energy for Constant Time of Flight to Equator
b
Launch=0°
Lobs=5.9
λobs=21°
E(eV)
200
150
100
50
0
0
30
60
90
120
150
180
Local Pitch Angle

Figure 9b

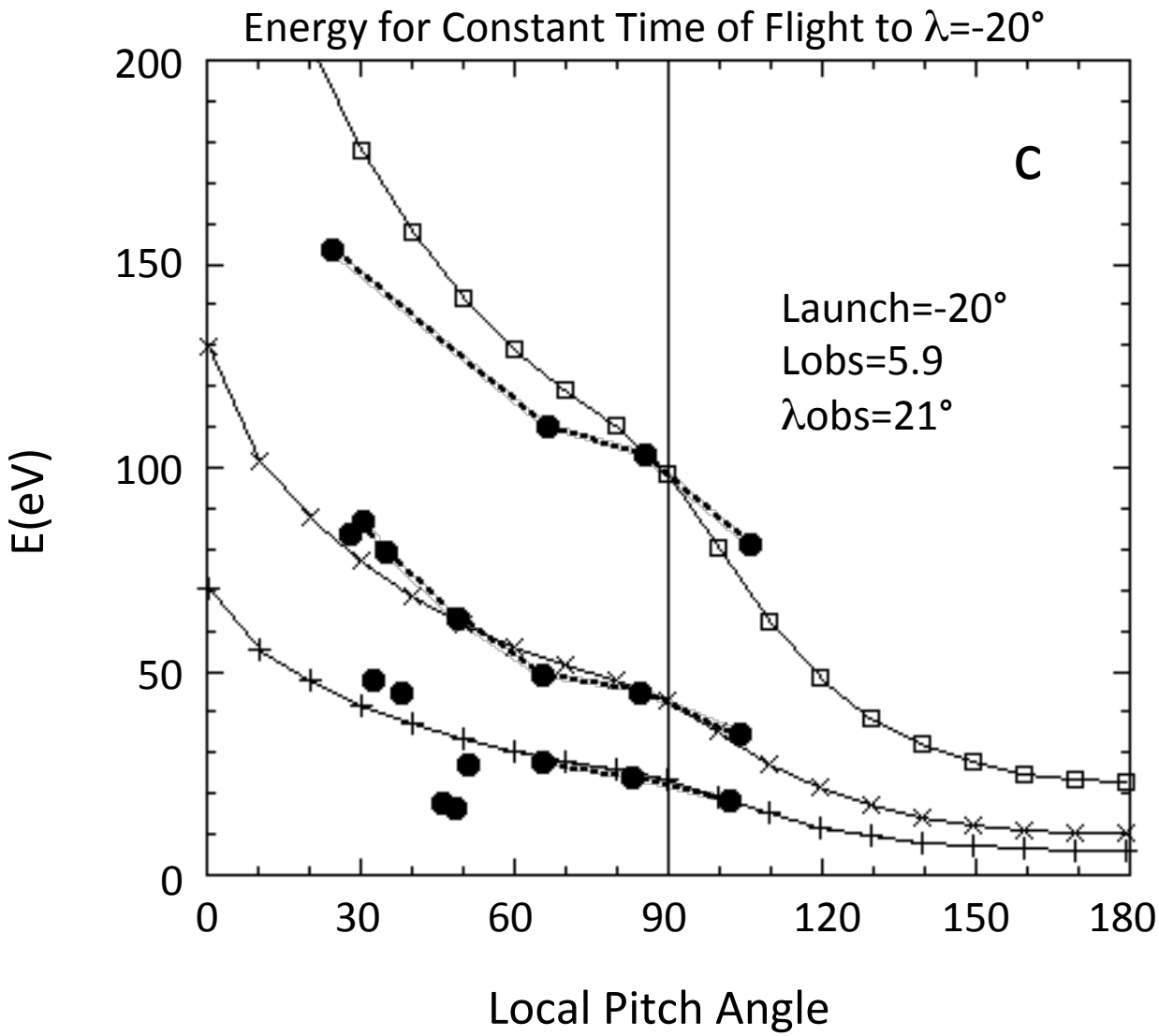
Energy for Constant Time of Flight to λ=-20°
C
Launch=-20°
Lobs=5.9
λobs=21°
E(eV)
200
150
100
50
0
0
30
60
90
120
150
180
Local Pitch Angle

Figure 9c

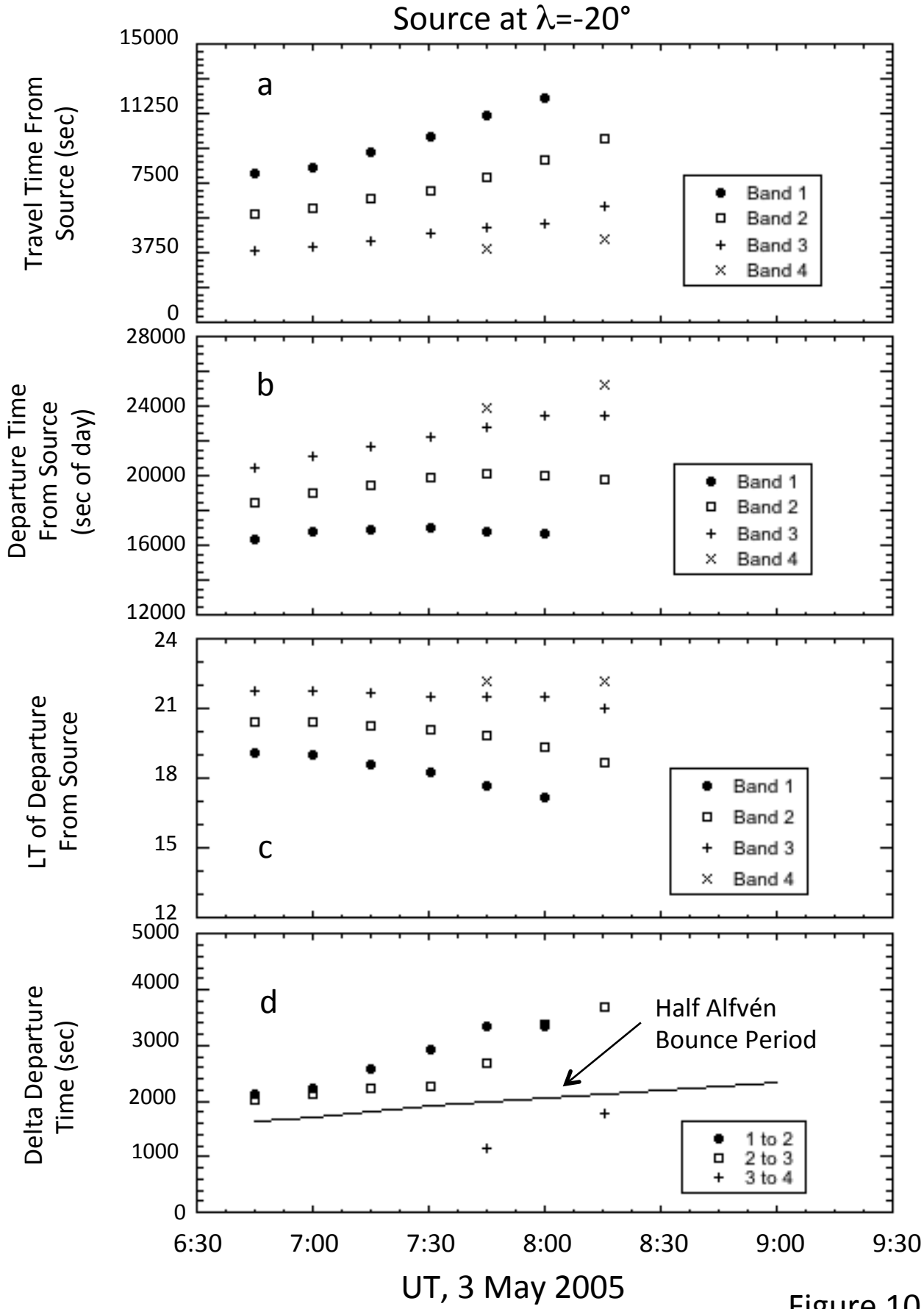
Source at λ=-20°
Travel Time From Source (sec)
15000
11250
7500
3750
0
a
Band 1
Band 2
Band 3
Band 4
Departure Time From Source (sec of day)
28000
24000
20000
16000
12000
b
LT of Departure From Source
24
21
18
15
12
c
Delta Departure Time (sec)
5000
4000
3000
2000
1000
0
d
Half Alfvén Bounce Period
1 to 2
2 to 3
3 to 4
6:30
7:00
7:30
8:00
8:30
9:00
9:30
UT, 3 May 2005

Figure 10

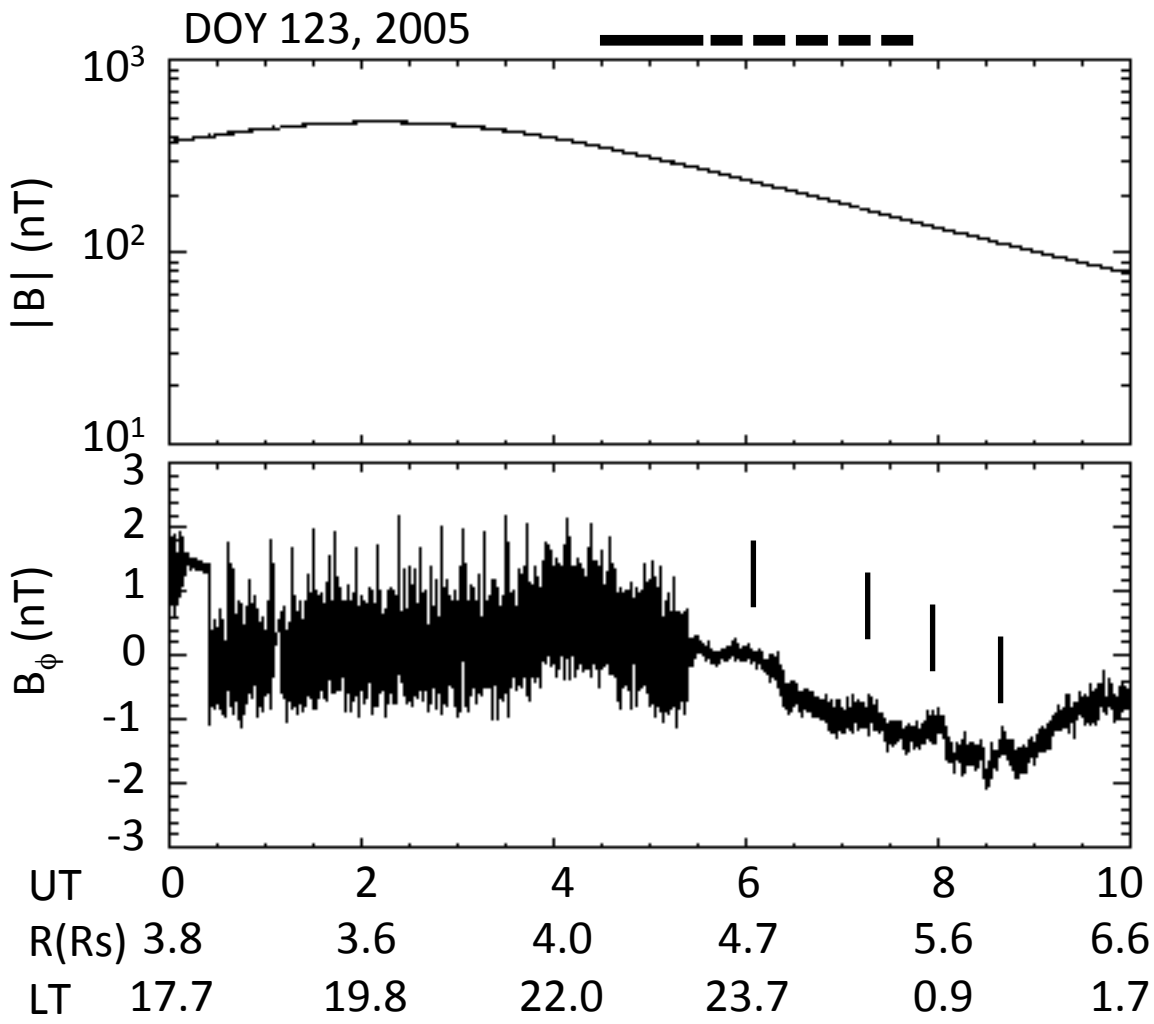
DOY 123, 2005
10^3
10^2
10^1
|B| (nT)
3
2
1
0
-1
-2
-3
B_ϕ (nT)
UT 0 2 4 6 8 10
R(Rs) 3.8 3.6 4.0 4.7 5.6 6.6
LT 17.7 19.8 22.0 23.7 0.9 1.7

Figure 11a

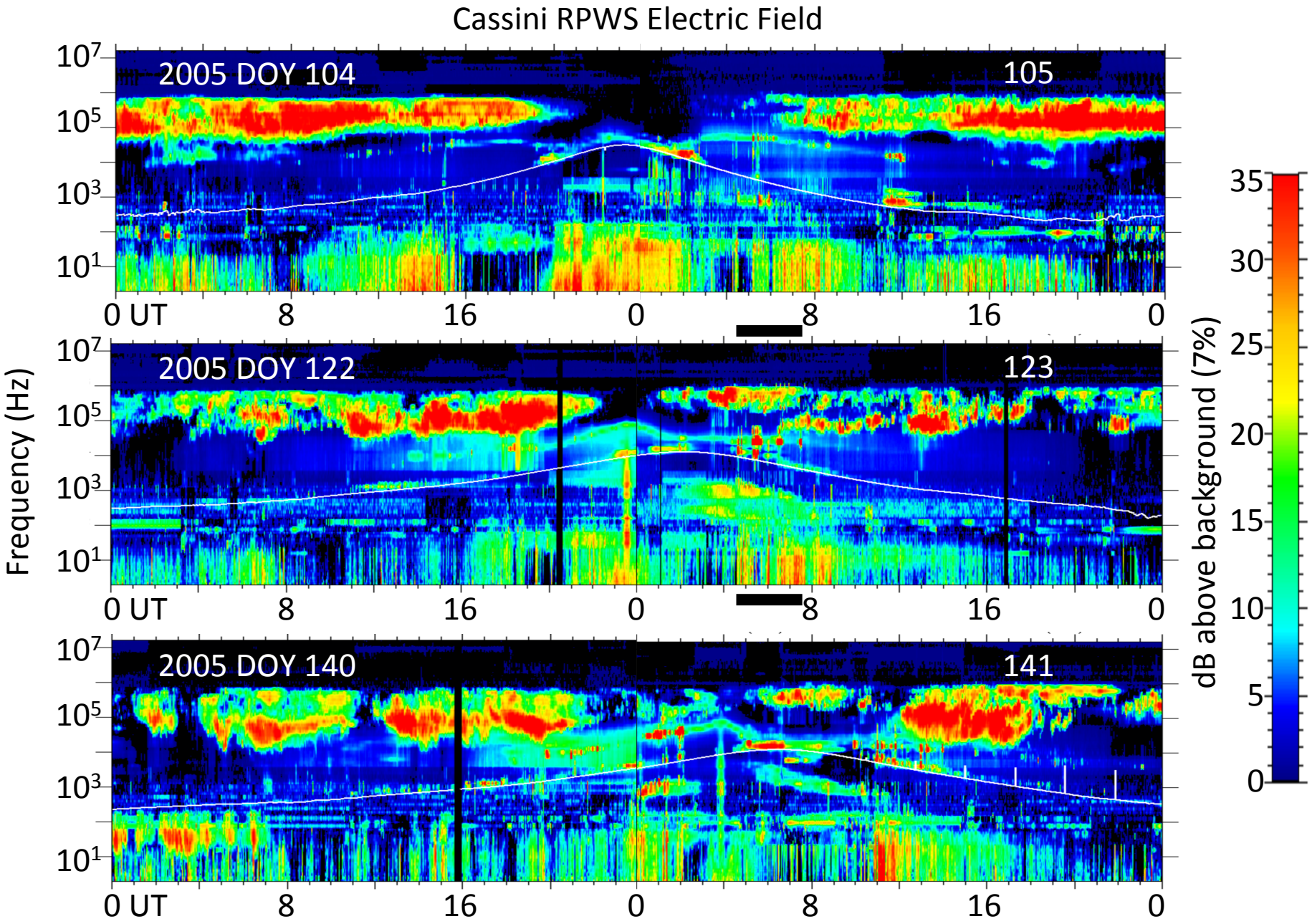
Cassini RPWS Electric Field
2005 DOY 104
105
2005 DOY 122
123
2005 DOY 140
141
Frequency (Hz)
10^7
10^5
10^3
10^1
0 UT
8
16
0
dB above background (7%)
35
30
25
20
15
10
5
0

Figure 11b

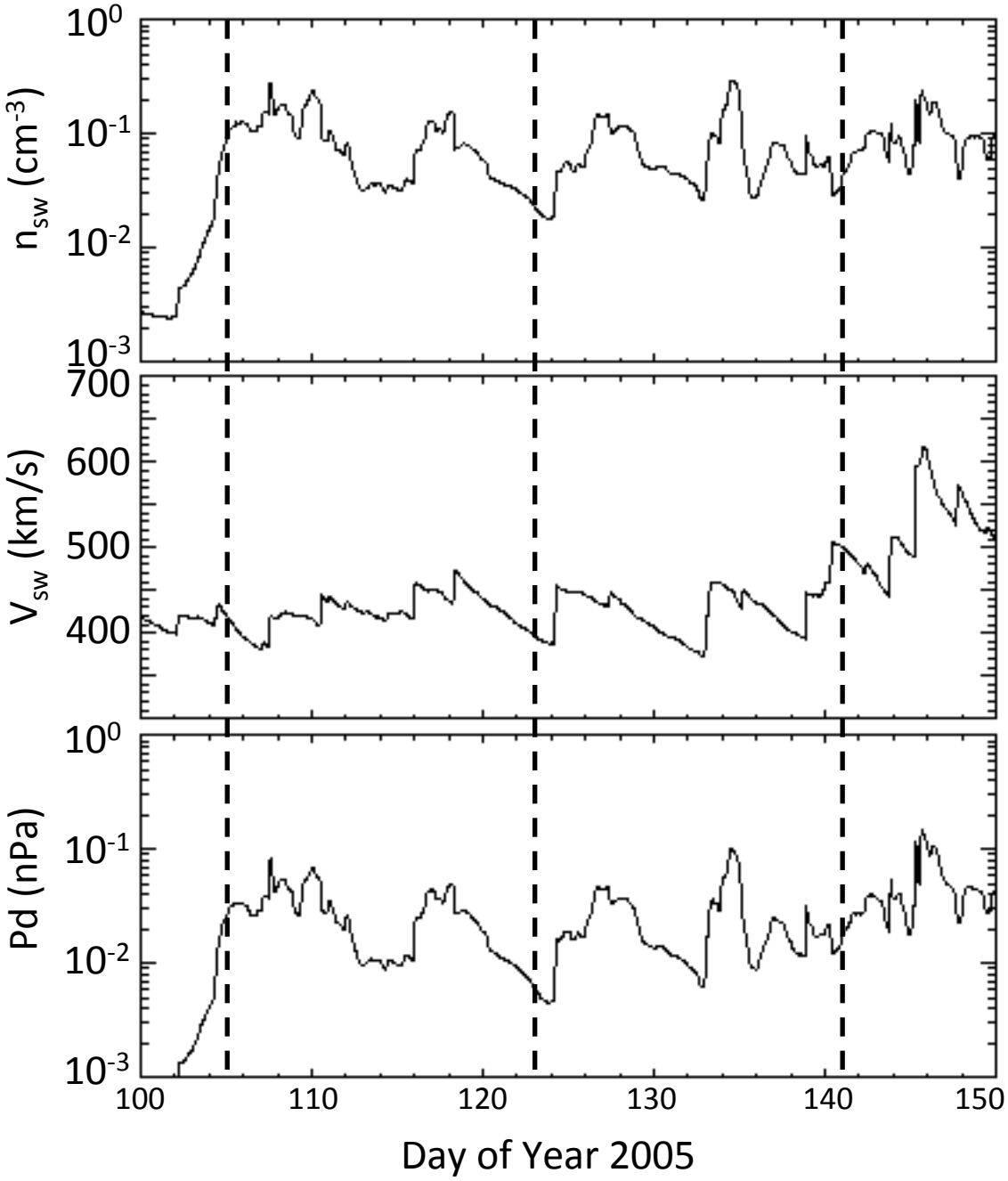
10^0
10^{-1}
10^{-2}
10^{-3}
n_{sw} (cm^{-3})
700
600
500
400
V_{sw} (km/s)
10^0
10^{-1}
10^{-2}
10^{-3}
Pd (nPa)
100
110
120
130
140
150
Day of Year 2005

Figure 11c